Thermoforming process effects on structural performance of carbon fiber reinforced thermoplastic composite parts through a manufacturing to response pathway

Madhura Limaye[1#], Sai Aditya Pradeep[2,3#], Anmol Kothari[1], Sushil Savla[2,3], Akshat Agha[5], Srikanth Pilla[1,2,3,4] ,Gang Li[1*]

[1]Department of Mechanical Engineering, Clemson University, Clemson, SC - 29631, USA

[2]Department of Automotive Engineering, Clemson University, Clemson, SC - 29631, USA

[3]Clemson Composites Center, Clemson University, Greenville, SC - 29607, USA

[4]Department of Materials Science & Engineering, Clemson University, Clemson, SC - 29634, USA

[5]FADI-AMT LLC, Greenville, SC - 29607, USA

*Author to whom correspondence should be addressed. Electronic mail:

# Authors contributed equally to this work

Abstract

Thermoforming process of thermoplastic-based continuous CFRP's offer a major advantage in reducing cycle times for large-scale productions, but it can also have a significant impact on the structural performance of the parts by inducing undesirable effects. This necessitates the development of an optimal manufacturing process that minimizes the introduction of undesirable factors in the structure and thereby achieves the targeted mechanical performance. This can be done by first establishing a relationship between the manufacturing process and mechanical performance and successively optimizing it to achieve the desired targets. The current study focuses on the former part, where a manufacturing-to-response (MTR) pathway is established for a continuous fiber-reinforced thermoplastic composite hat structure. The MTR pathway incorporates the thermoforming process-induced effects while determining the mechanical performance and principally comprises of material characterization, finite element simulations, and experimental validation. The composite material system selected for this study is AS4/Nylon-6 (PA6) with a woven layup. At first, the thermoforming simulations are performed above the melt temperature of PA6 using an anisotropic hyperelastic material model, and the process-induced effects such as thickness variation, fiber orientations, and residual stresses are captured from the analysis. Residual stresses developed in the formed structure during quench cooling from the elevated temperature are predicted by the implementation of classical laminate theory (CLT). These results are then mapped onto a duplicate part meshed suitably for mechanical performance analysis. A quasi-static 3-point bend test and a dynamic impact test are carried out and the results are compared with experimental tests. Experimental results from thermoforming, bending and dynamic impact trials show good agreement with the simulation results for the hat structure under consideration. Further, the static and dynamic performance is evaluated for the thermoformed structure and the effects of the thermoforming process are compared numerically, for the cases with and without the inclusion of process effects.

Keywords: *Thermoforming, finite element analysis, thermoplastic composites, residual stress*

1. Introduction

The automotive industry has witnessed a remarkable shift in materials in the past few decades. For instance, the usage of polymers and discontinuous fiber-reinforced polymer composites for aesthetic and non-structural applications have increased from 9 kg per car in the 1960s to 162 kg in 2010 [1]. Over the past decade, the industry has seen increased interest in adopting thermoset-based continuous carbon fiber reinforced polymer (CFRP) composites for structural applications [2–6]. For example, recently BMW i3 used carbon fiber-based thermoset composite material for their Body-in-White (BIW) which is manufactured using high-pressure resin transfer molding (HPRTM). These thermosets-based CFRP's while being extremely stiff, suffer from a variety of challenges such as relatively higher cycle times, non-recyclability, increased capital expenditure for HPRTM equipment, and its brittle behavior. A new and upcoming alternative to this paradigm that has gained enormous attention from researchers and industry alike is the use of thermoplastic-based continuous CFRPs processed using the thermoforming or compression molding route [7,8]. This is primarily in part due to the numerous benefits of this approach including: (i) shorter cycle time, (ii) recyclable material, (iii) compatible with existing stamping lines (only minor modifications are required), (iv) higher ductility [9]. As the development of continuous carbon fiber reinforced thermoplastic (CFRTP) composite structures or structural components can be accelerated by using computational engineering approaches, design optimization [10,11] or manufacturing optimization [12,13] studies have been conducted on CFRTP composites. It was shown that optimal strength and impact performance or optimum processing window for parameters such as stamping pressure, velocity, temperature and degree of crystallinity can be achieved. Nevertheless, while these analyses and optimizations are useful for their specific purposes, they are largely isolated and disconnected from each other. Such compartmentalized approaches have a fundamental drawback in the design and optimization of CFRTP structures. This is due to the fact that the material properties and mechanical behavior of CFRTP is intrinsically coupled with the thermoforming/compression molding process, leading to inhomogeneous fiber orientations, thickness variations, and residual stresses in the formed CFRTP structures. These process-induced effects can have a significant influence on CFRTP composite structures' mechanical response [14–17]. For example, fiber reorientations and the resulting changes in material properties have shown a considerable impact on static structural performance [14–16]. In another study, the cooling rate which directly influences the magnitude of residual stresses generated in the formed part was shown to affect the mechanical performance [17]. Therefore, in order to develop high performance, high-quality CFRTP composite structural components, an integrated design and manufacturing optimization approach is required.

Such an integrated approach can be achieved by first establishing a relationship between the manufacturing process and mechanical response of the structure, and successively, optimizing the manufacturing process parameters to achieve the desired targets. This requires the development of a pathway (or CAE chain) comprising of computational models for all the process steps which are validated with experiments at coupon and structural level. To this end, a few attempts have been made to connect the design, manufacturing and structural simulation steps in series, by developing virtual process chains (CAE chains) and mapping methods [16,18,19]. However, the recent publications implementing these methods have failed to consider some of the relevant effects or steps of the manufacturing process. For example, Kärger et al. [19] developed a comprehensive CAE chain for the RTM process of thermoset-based composites which involves draping, molding, and structural analysis steps, but it lacked curing simulation, which is a vital part of modeling the physics of the RTM process. It is important to note that a complete CAE chain would involve curing simulation in the case of thermoset processing and cooling simulation in the case of thermoplastic processing. In a separate study, Hsiao et al. [20] developed a FE model to determine the effect of both forming and cooling processes on CFRTP. While the process-induced effects such as thickness distribution, fiber orientation, and residual stress development are presented for various part shapes, they did not investigate the effects of these results on the structural response. A notable contribution has been made by Jayasree et al. [21] employing extensive simulation and experimental methods to study a hybrid (forming + injection molding) molding process. Their model involves FE analysis, experimentation, and validation at each level i.e. coupon level, structural level, and system-level based on a "Building block approach" developed by NASA [22]. At the structural level, process-induced effects are included to determine the structural response. However, in their work, cooling-induced residual stresses are not incorporated which can significantly affect the response of the thermoformed structure under static and dynamic loading. Specifically, for the thermoforming process of CFRTPs, a pathway that considers all the relevant process steps i.e. thermoforming, cooling, and structural analysis is not yet developed.

The present work establishes a complete manufacturing-to-response (MTR) pathway for end-to-end analysis of thermoformed continuous carbon fiber reinforced Polyamide 6 (PA6) composite asymmetric hat structure. This geometry was chosen as a subcomponent that formed the sash region of a thermoplastic door that is currently in development and the fact that real-world use of thermoplastic composites necessitates understanding the forming process for a geometrically complex profile. This pathway comprises of numerical simulation of the thermoforming process of CFRTP composites and their experimental validation from coupon to the structural level which is carried out in five process steps described in Section 2. The MTR pathway contributes towards building confidence in process simulations which will reduce the product development time of CFRTP based structures and lead to their widespread adoption in the future. To the best of the authors' knowledge, this is the first synergistic experimental and

numerical approach that wholly captures process-induced effects and their impact on static and dynamic mechanical performance. The remaining paper is organized as follows. A detailed description of the proposed MTR pathway is provided in Section 2. Experimental procedures adopted for material characterization as well as the thermoforming and mechanical tests are detailed in Section 3. The modeling and numerical simulation steps in the pathway are described in Section 4. Results and discussions are presented in Section 5. Finally, conclusions and future work based on current limitations are presented in Section 6.

2. Manufacturing-to-response pathway

Figure 1 shows the general framework of the MTR pathway which consists primarily of five process steps as follows: 1) material characterization at coupon level and material card (MAT card) generation for thermoforming simulation and mechanical analysis, 2) thermoforming simulation and experimental validation at the structural level, 3) experimental and numerical cooling analysis followed by residual (skin/core) stress analysis, 4) mapping of process-induced effects and 5) mechanical performance evaluation and experimental validation at the structural level. The detailed steps of the MTR pathway are described here.

In the first step, material properties at the coupon level are experimentally characterized. These properties are used to generate material cards for performing numerical simulations such as thermoforming and cooling simulation, residual stresses analysis, and mechanical analysis. Typically, the thermoforming process is carried out at a temperature above the melting point of the resin. Thus, material testing at coupon level is conducted above the melt temperature of PA6 (>220°C) to determine tensile and shear mechanical properties. The thermal characteristics of the material such as thermal conductivity and coefficient of thermal expansion are determined for cooling analysis and residual stresses calculation. Additionally, tensile tests are conducted at 60°C, 110°C and 170°C to obtain tensile moduli for residual stress calculation. Finally, room temperature tensile and compression tests are carried out to obtain the mechanical properties to perform static and dynamic mechanical analysis. The second step of the pathway comprises of thermoforming experiments and simulations. The thermoforming experiments are conducted at near isothermal conditions. Thermoforming simulations are performed using the material card developed in Step 1. The changes in fiber orientations and thickness variations obtained from the simulations are validated with the experimental results in this step. The third step consists of quench cooling experiment, FE cooling analysis, and calculation of cooling induced residual stresses. In this step, the thermoformed structure is first cooled by forced convection till 100°C and further quench cooled to room temperature by using forced flow cooling and the temperature evolution of tools during cooling is recorded. These cooling curves are used as an input boundary condition to carry out the transient cooling FE analysis. The spatial

temperature distribution and evolution are obtained for the thermoformed composite structure from the FE cooling analysis, which is then used as an input, to compute the cooling induced residual stresses. In the fourth step, the predicted residual stresses, thickness variations, and fiber reorientations are incorporated into the static and dynamic FE setup, by using a mapping procedure. The last step of the MTR pathway involves numerical evaluation of the mechanical response under the static and dynamic loading conditions which is validated by the experimental tests. In this study, a quasi-static three-point bend test and a dynamic impact drop tower test is considered to validate the process-induced effects on the mechanical response by comparing the deformation, stresses, and failure characteristics. Impact drop tower test is considered to validate the process-induced effects on the mechanical response by comparing the deformation, stresses, and failure characteristics.

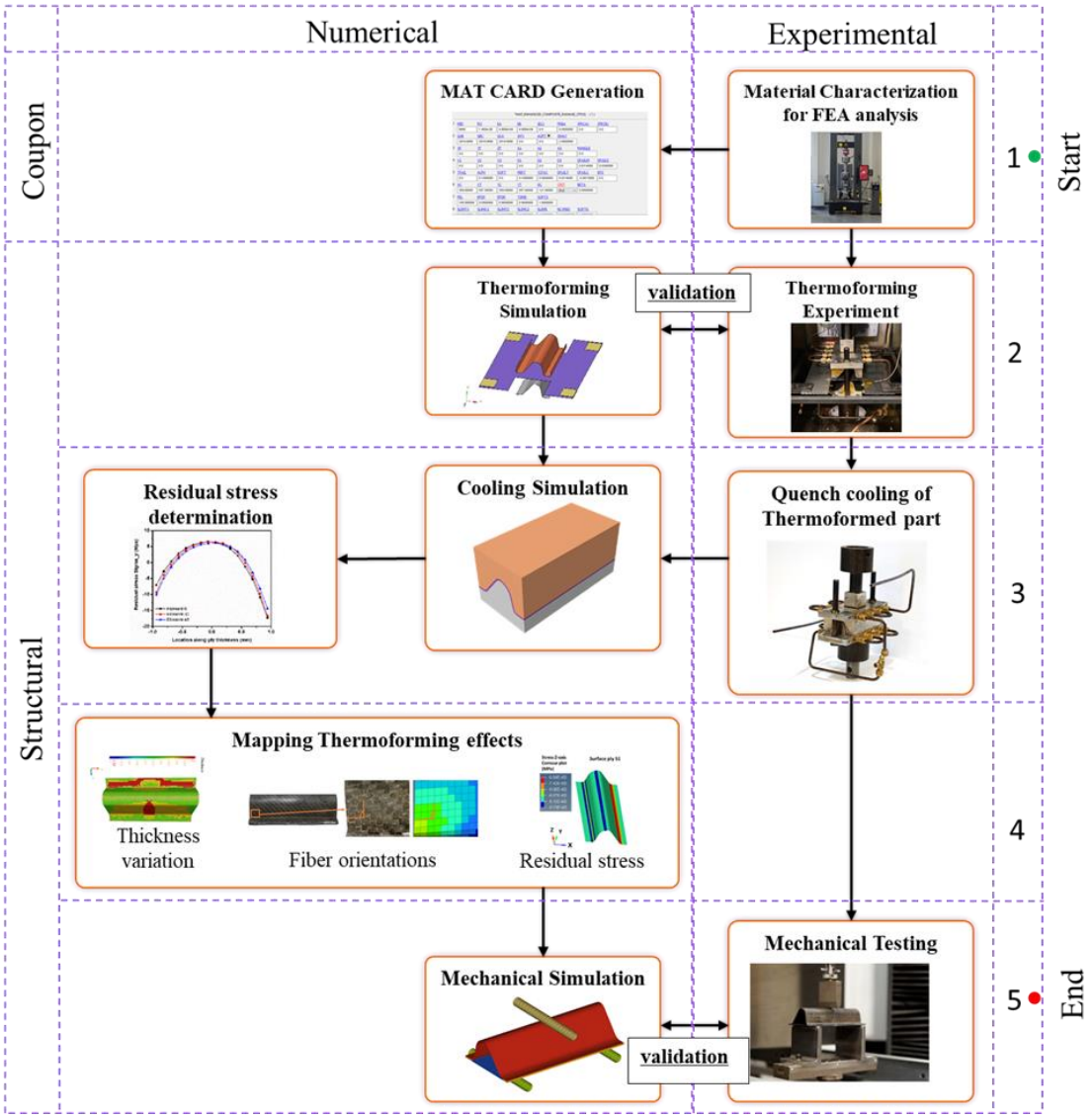

Figure 1 Manufacturing-to-response (MTR) pathway.

3. Experimental setup for material characterization and model validation

The material considered for the current study is carbon fiber reinforced PA6 2*2 twill weave laminate of 1.97mm thickness. The fiber content by volume is 50 wt. %. Considering the balanced weave of the material, in-plane properties are assumed to be equivalent in the warp and weft directions.

3.1 Material characterization for thermoforming analysis

High temperature above the melting point of PA6 (>220°C) tests are conducted in 0/90 and +45/-45 orientations for which samples are waterjet from the pre-consolidated sheets received from the supplier. Test samples in 0/90 orientation measure 180 mm in length, 25 mm in width, and 1.97 mm in thickness, while samples in +45/-45 orientation measure 250 mm in length, 25 mm in width and 1.97 mm in thickness. As per ASTM D 3039, a crosshead speed of 5 mm/min is used on at least 5 samples.

The method used for tensile testing of the +45/-45 orientation samples at high temperature is termed as the bias-extension test. A normal force vs displacement plot is obtained from the bias-extension test (see Appendix A1), which is converted to shear stress vs shear angle plot. The process is illustrated herein. Consider the specimen under a bias-extension test, with three zones of deformation as shown in Figure 2. The zone A largely remains undeformed during the test while the zone B undergoes both tensile and shear deformation. The zone C undergoes pure shear deformation which is used for the determination of shear characteristics of the composite material. The angle $\theta_o = 45°$ is the initial configuration of zone C while θ defines the deformed angle. The shear angle γ in zone C can be expressed as [23]:

$$\gamma = 90° - 2\theta = 90° - 2\cos^{-1}\left(\frac{L_{eff}}{\sqrt{2}L_0}\right) = 90° - 2\cos^{-1}\left(\frac{L_0 + \delta}{\sqrt{2}L_0}\right) \tag{1}$$

where $L_0 = H - W$, H is the initial height and W is the initial width of the specimen, δ is the displacement recorded during the test. The normal force obtained from the bias-extension test is converted to normalized shear force by applying a normalization technique proposed by Harrison et al. [24] for rate-dependent materials. The normalized shear force as a function of shear angle is given as [23]:

$$F_{sh}(\gamma) = \frac{\left(\frac{H}{W} - 1\right)}{\left(2\frac{H}{W} - 3 + 2X\right)} \frac{F}{\frac{\sqrt{2}W}{2}} \tag{2}$$

where $X = \frac{1}{4}\left\{\frac{cos^2(\gamma)(1+3sin^2(\gamma/2))}{cos^2(\gamma/2)(1+3sin^2(\gamma))}\right\}$. The shear force calculated using Equation (2) is divided by the thickness (1.97mm) of the specimen to give the shear stress. The high temperature (HT) shear modulus is thus calculated from the shear stress-shear angle plot.

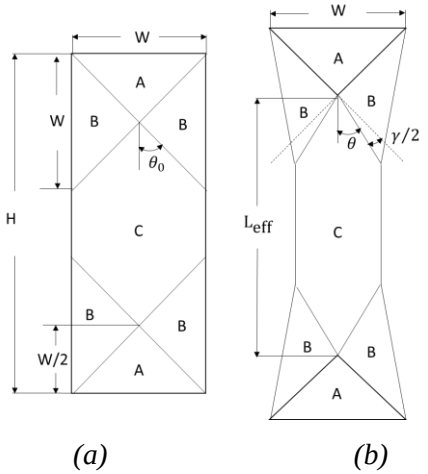

Figure 2 Composite specimen under the bias-extension test (a) undeformed and (b) deformed configurations (after Lebrun et al. [25]*).*

3.2 Material characterization for cooling analysis and residual stresses calculation

The thermal properties including thermal conductivity, specific heat capacity, and coefficient of thermal expansion (CTE), are experimentally determined for the carbon/PA6 composite material under investigation. The thermal conductivity of composite samples is measured as per ASTM D 7984 using a C-Therm TCi TH91-13-00703 instrument. Three tests are performed on the samples having dimensions 8 mm (length) × 8 mm (width) × 1.97 mm (thickness). Specific heat capacity is determined in accordance with ASTM E 1269 on three circular composite samples (6 mm diameter and 1.97 mm thickness). The tests are performed on a DSC Q 20 (TA instruments). Sapphire standard, empty pans, and composite samples are tested from 20 °C to 60 °C at a ramp rate of 10 °C/min under nitrogen atmosphere and an average result of three samples are reported in Table 1. CTE is determined by conducting the probe expansion measurement on a TMA Q 400 (TA instruments). Measurements are performed on samples having a size of 8 mm (length) × 8 mm (width) × 1.97 mm (thickness). Three samples are tested from -30 °C to 60 °C at a ramp rate of 10 °C/min under nitrogen atmosphere. The thermal properties experimentally obtained are listed in Table 1. It is important to note that viscoelastic effects are dominant above the glass transition temperature of PA6 (Tg = 60°C) (Refer section 4.2). The CTE values below and above Tg are determined experimentally. An average CTE value in both the warp and weft directions is determined to be 1.54e-6 /°C below Tg and 1.86 e-6 /°C above Tg.

The temperature-dependent elastic moduli of the material are required for the calculation of residual stresses. The uniaxial tension tests are performed on the material in 0/90 and 45/-45 direction at 25°C, 60°C, 110°C, and 170°C (refer Appendix A2). The tests are conducted on a specialized setup where a custom furnace is placed over an Instron 5985 universal testing machine with a 250kN load cell. The furnace has a

glass window opening on one side, which allows optical strain measurements using digital image correlation. The point displacements are obtained using a high resolution, high framerate 16-megapixel camera, and the analysis is performed using GOM Correlate Professional software. The test samples are clamped using high-temperature hydraulic grips at a 100 mm grip to grip separation and are pulled at a crosshead speed of 1mm/min. The use of a custom setup incorporating DIC ensures accurate and repeatable elastic and shear modulus values, even at high temperatures, which are listed in Table 2.

Table 1. Material properties for cooling analysis

Property		**Carbon/PA6**	**6061-T6 Aluminum** [26]
Density $[kg/m^3]$		1430	2700
Specific Heat $[J/kg\ K]$	@ 25°C	1206.65 ± 24.57	896
	@ 45°C	1304.96 ± 21.36	
	@ 60°C	1364.76 ± 18.64	
Thermal conductivity $[W/m\ K]$ @ 25°C		0.682 ± 0.001	167

3.3 Material characterization for mechanical analysis

Material characterization is conducted in tension, compression, and shear using appropriate standards (refer Appendix A2). Tensile tests for the 0/90 direction are performed in accordance with ASTM D 3039 as described in Section 3.1 and 3.2. Compression tests are carried out for the 0/90 and +45/-45 samples per ASTM D 6641. Samples with the following dimensions: 140 mm (length), 13 mm (width) and 1.97 mm (thickness) for 0/90 and 150 mm (length), 25 mm (width) and 1.97mm (thickness) for +45/-45 orientation are waterjet. A uniaxial strain gauge is bonded on each side of the sample in order to measure the strain on both sides to ensure there is no buckling. All compression tests are performed on a combined loading compression (CLC) fixture on an Instron 5985 universal testing machine with a 250 kN 2580 series static load cell using a crosshead speed of 1 mm/min. The material properties obtained from the tests are listed in Table 2.

Table 2. Average mechanical properties for investigated woven Carbon/PA6 composite

Property		**Young's Modulus (GPa)**	**Shear Modulus (GPa)**	**Stress at Failure (MPa)**	**Strain at Failure (%)**
Tension 0/90°	@ 25°C	55.54 ± 0.62	NA	581.5 ± 27.7	1.00 ± 0.05
	@ 60°C	54.04 ± 0.62		464.2 ± 20.1	0.92 ± 0.05
	@ 110°C	50.83 ± 0.49		435.5 ± 37.7	0.97 ± 0.10
	@ 170°C	48.13 ± 0.80		417.1 ± 21.6	0.95 ± 0.06
	@ 264°C	34.20 ± 0.65		148.0 ± 7.0	0.94 ± 0.05
Tension 45°	@ 25°C	NA	1.783 ± 0.09	131.5 ± 6.7	45.47 ± 2.85
	@ 264°C		4.39e-6 ± 1.01e-6		
Compression 0/90°	@ 25°C	50.08 ± 13.23	NA	303.0 ± 16.0	0.631 ± 0.01
Compression 45°	@ 25°C	NA	1.4 ± 0.18	70.4 ± 2.0	31.93 ± 1.22

3.4 Experimental tests for model validation

The MTR pathway presented in this study is validated by first fabricating a composite hat structure using the thermoforming process and then by performing mechanical tests. The experimental measurements are then compared with the numerical results. The experimental tests are discussed here.

3.4.1 Hat section fabrication (thermoforming setup)

The thermoforming setup consists of two forming tools (punch and die) and the blank holder apparatus accommodated in a thermal chamber shown in Figure 3(*a*). A rigid steel frame is constructed to hold the composite sheet (blank) with the help of binder tabs of size 70 mm ×38 mm at four locations. The sheet is held in place with an initial blank holder force of 70 N. All forming tests are carried out on Instron 5985 universal testing machine with a 250 kN 2580 series static load cell. Tests are carried out using a crosshead speed of 5 kN/min speed till the pre-set load of 22 kN is reached. The mean pressure of thermoforming is estimated to be 1.97 MPa. The entire set up including the frame, blank and forming tools are placed in the furnace, thermocouples are placed on the punch, die, blank and the furnace is heated to 264°C. The thermocouple readings for the tools and the blank recorded using an e-DAQ during the heating phase are shown in Figure 4. The blank is thermoformed to a hat structure at close to isothermal conditions within the narrow forming window (Figure 4). After the thermoforming process, the entire setup is then cooled via forced convection till the hat structure reaches 100 °C. Subsequently, liquid nitrogen is injected through

copper cooling channels in the tool in order to quench cool the formed structure to room temperature. The thermocouple readings for punch, die, and hat structure during the cooling phase are shown in Figure 4. The intent of quench cooling is to demonstrate the effect of cooling rate of the tools on the formation of residual stresses in the structure. Since the thermocouple measuring hat structure temperature is not placed between the punch and die, its cooling data does not provide accurate temperature evolution in the formed hat structure. As a result, the hat structure cooling data cannot be used directly for residual stress determination. Nevertheless, the thermocouple measurement serves as a useful reference to initiate and stop the thermoforming process when the desired temperature values are reached. The cooling channels (see Figure 3(b)) are constructed in such a way that the hat structure does not come in contact with the liquid nitrogen, any cooling seen on the material is due to conduction from the punch and die tools. The fabricated hat structure has a width of 75 mm and length of 145 mm, the hat cross-section view and side view is shown in Figure 3(b). To the best of the authors' knowledge, this work is the first that uses in-mold liquid nitrogen cooling to quench cool a composites part after forming.

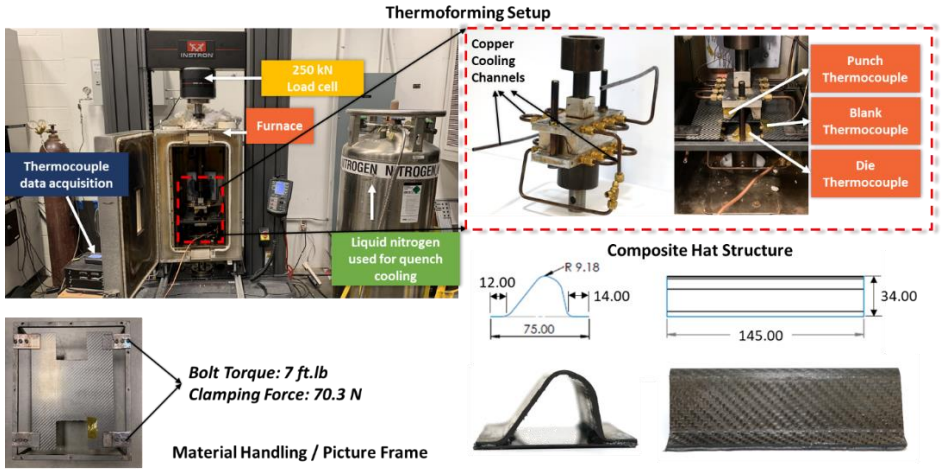

(a) *(b)*

Figure 3 (a) Thermal chamber equipped with thermocouple data acquisition system and liquid nitrogen cooling for thermoforming tests, material handling system with binder tabs holding the blank. (b) thermoforming setup showing copper cooling channels, thermocouple locations and thermoformed hat structure in cross-section view and side view.

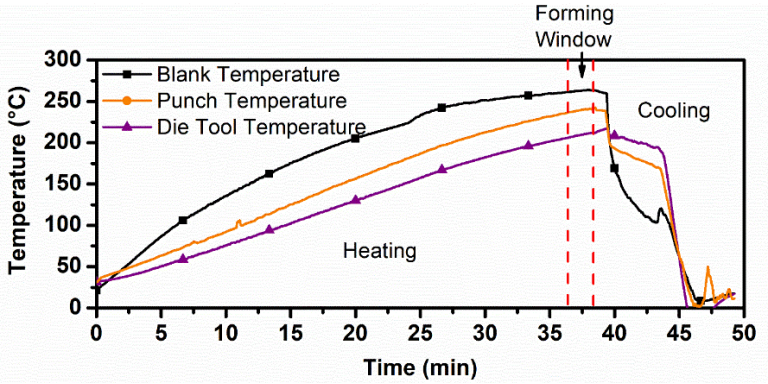

Figure 4 Thermocouple data for punch, die and blank during thermoforming process showing heating, forming and cooling phases

3.4.2 Three-point bend test

The hat structure samples are adhesively bonded to a 0.5 mm thick woven carbon/PA 6 composite sheet using the Plexus MA 530 adhesive material as shown in Figure 5(*a*). The experimental setup for the quasi-static three-point bending test with the bonded hat structure is shown in Figure 5(b) which consists of two supports with the span of 119.3 mm and a punch. The tests are carried out on Instron 5985 universal testing machine with a 10 kN 2580 series static load cell using a modified 2810 series flexure fixture from Instron. The three-point bend tests are conducted on three samples with a crosshead speed of 1 mm/min.

3.4.3 Dynamic Tests

The formed hat structures are secured in aluminum plates as shown in Figure 5(c) to fix the flanges of the hat structure. The experimental setup for these dynamic tests consists of two constraints that are 20 mm long and a 1-inch diameter punch having an overall weight of 3.1 kg, The tests were carried out on a Lansmont Corporation cushion testing machine equipped with a 2000 g PCB accelerometer TP3 data analysis software, Olympus i-Speed 3 high-speed camera. The dynamic tests are conducted on three samples with an average drop speed of 4.3 m/s.

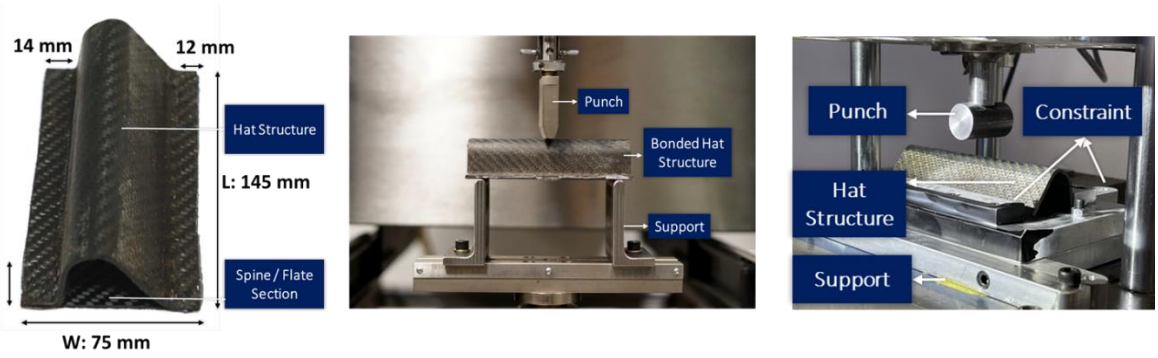

(a) *(b)* *(c)*

Figure 5 (a) Dimensions of bonded hat structure (b) Experimental setup for 3-point bend test showing the bonded hat structure, supports and punch (c)Experimental setup for dynamic tests showing the constrained hat structure, support, constraints and punch.

4. Modeling pathway

The FE model for thermoforming process is developed to reproduce the experimental setup. The thermoforming simulation process is broken down into two steps. In the first step,–thermoforming simulations are performed using material properties for the blank at forming temperature (264℃). In the second step, the cooling analysis is performed in closed mold till room temperature condition is reached. The heat transfer analysis through the hat structure and development of thermal stresses during the cooling process is modeled and simulated as two stages of the cooling step.

4.1 Thermoforming simulation

The FE setup to perform thermoforming simulation is shown in Figure 6, which consists of punch, die, and four binder tabs to hold blank similar to experiments. The punch, die and binder tabs are modeled as rigid bodies using thin shell elements. The blank is oriented in 0/90 configuration with respect to the punch and die. Four pairs of binder tabs are used to support the blank of which four tabs below the blank are fixed. Each binder tab above the blank (visible in Figure 6(*a*)) applies a constant load of 70N on the blank (along Y-axis) to hold it in place during forming. To form the blank, the punch travels towards the die till the mold closes completely. The interface between the tools and the blank is modeled as a penalty-based friction contact [27]. The coefficient of friction of 0.2 is selected from a narrow range of values reported previously for forming simulations [28,29].

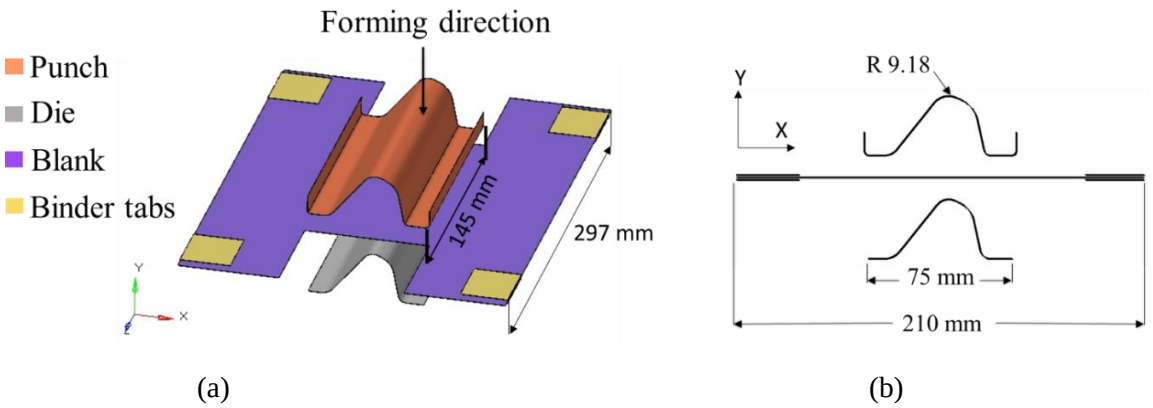

Figure 6 (a) Finite element model for forming simulations showing components namely punch, die, blank, binder tabs and forming direction, (b) dimensions and arrangement of components in cross-section view

The thermoforming simulations are performed in HyperForm using RADIOSS, a finite element solver developed by Altair Engineering. The composite blank material behavior is modeled with MAT LAW 58 which is an anisotropic hyperelastic fabric material model. In the forming analysis, it is assumed that the strain energy is consumed in the blank deformation only during loading (travel of punch towards die), and the un-loading effect is not considered [30],[31-33]. The thickness of the blank is defined to be 1.97 mm and modeled with fully integrated QBAT shell elements with a mesh size of 2 mm. Tensile and shear moduli used as inputs to MAT LAW 58 are listed in Table 2 and are calculated from high-temperature material characterization data. A bending factor of 0.0015 is defined to relax the tensile stiffness of the fibers in compression mode. It should be noted that the anisotropic hyperelastic fabric material model MAT LAW 58 is employed in this study because the forming is under close to isothermal conditions, which means there is no need to consider the thermomechanical effect in this simulation step. The development of thermal stresses during the cooling process is modeled and simulated in a separate step. In addition, the accuracy of the MAT 58 model is ensured as the shear and tensile properties used in the model are obtained by characterizing the composite specimen itself at the forming temperature. Our results show that the model is capable of predicting shear angles and potential sites of wrinkling, which are important for further simulations in the pathway.

4.2 Cooling analysis

During the thermoforming process, internal residual stresses are induced when the formed part, which is still held in position by the punch and die, is cooled to the service temperature. A comprehensive review of residual stresses formation in thermoplastic composites can be found in [34–36], and a brief literature review is discussed here. Typically, process-induced residual stresses on CFRTP are presented at different length scales of the composite architecture, namely the micromechanical, macromechanical, and “global”

level [37]. At the micromechanical level or fiber/matrix interaction level, these stresses are primarily influenced by the difference in properties of fiber and matrix, such as CTE and Young's modulus mismatch, and the fiber/matrix interfacial bond strength. The nature and effects of residual stresses at the micromechanical level have been studied extensively for heat-cured thermosets [38,39] and thermoplastics and can be determined using both numerical techniques such as mean-field homogenization techniques [20] and experimental techniques such as Raman microscopy and photoelasticity presented in [40,41]. While stresses at this level can result in failure at the fiber-matrix interface, they are beyond the scope of the current study as it will require multiscale modeling of composite behavior. At macromechanical or ply/ply interaction level, the residual stresses mostly arise due to anisotropic shrinkage of lamina during the cooling phase which majorly affects unbalanced laminate structure [37,42–44]. However, since a balanced composite layup is investigated here, therefore, macromechanical stresses arising in an unbalanced layup are also neglected. At the "global" level, i.e. in case of a thick laminated structure, thermal skin-core stresses are developed along the thickness of the laminate, during the cooling phase [45,46]. These stresses are primarily developed due to the difference in cooling rate between center and surface plies, resulting in a thermal gradient through thickness. In the present study, the thermal skin/core stresses at "global" level are considered, which occur due to the development of through-thickness thermal gradient during cooling phase. These stresses are evaluated in two steps. In the first step (Section 4.2.1), a heat transfer analysis is performed to determine the through thickness temperature evolution in the blank, during the cooling phase. In the second step (Section 4.2.2), the residual skin-core stresses are calculated by incorporating the through thickness temperature evolution data and implementing classical laminate theory-based thermomechanical analysis presented by [46,47].

The thermoforming process is carried out at the temperature (T) above the melting point of PA6 matrix i.e. at $T > 220°C$. At this elevated temperature, the structure is assumed to be in a 'stress-free' state and the stresses developed during forming are assumed to reduce to zero in the closed mold [20]. While cooling from melt temperature (Tm = 220°C) till the glass transition temperature (Tg = 60°C), the PA6 matrix undergoes viscous and viscoelastic phases. PA6 is a semi-crystalline polymer and as a result, crystallization occurs over a range of temperatures while cooling. The initiation of crystallization for PA6 matrix occurs at 172°C called as the crystallization temperature (Tc) [48]. Above Tc the PA6 matrix is in viscous phase where all generated stresses are assumed to relax out [46,49]. While below Tc and up to Tg, the PA6 matrix is in a viscoelastic phase [46]. Viscoelastic effects caused in this phase have been reported to cause stress relaxation during cooling [46,49,50]. As a result, these effects need to be accounted for while calculating the stress buildup in the structure from Tc to Tg. It is important to note that the fiber phase properties are thermally independent, as a result, the residual stresses builds-up instantaneously in the woven fibers while viscoelastic effects are observed in the matrix phase only. To accurately estimate the residual stresses at the

fiber/matrix interface, a micromechanical study is required [20,46]. However, the MTR pathway presented in this article focuses on the macro-level modeling approach to reduce the computational cost. Accordingly, the effective bulk properties of the composite lamina which depend upon both the temperature and degree of crystallinity are considered for calculating the residual stresses. A uniform degree of crystallization is assumed across the laminate at any given temperature. Further, temperature-dependent modulus of the laminate is obtained through material characterization. Details of the characterization are provided in section 3.2. It is assumed that below Tg, the structure behaves linear elastically till room temperature [49] and the residual stresses are calculated by considering temperature independent laminate properties.

4.2.1 Heat transfer analysis

The transient heat transfer analysis is performed to identify through-thickness thermal gradient in the laminated hat structure. The model setup in the global coordinate system (x, y, z) is shown in Figure 7(*a*), where the laminated composite hat structure is constrained by the punch and die (closed mold) during the cooling process. The surfaces of blank and the tools are assumed to be in uniform contact thereby, a uniform temperature distribution, along the length of the hat structure (along z-axis) is assumed. Consequently, the three-dimensional heat transfer analysis can be simplified for computational efficiency, into a two-dimensional (x, y) analysis, as shown in Figure 7(*b*). The analysis is carried out using FEM. The punch and die are discretized with a mesh size of 2mm. The laminated hat structure is discretized with an average mesh size of 0.123mm in the through-thickness direction and 2mm along the hat cross-section profile. The FE discretization of the laminated hat structure is illustrated in Figure 7(*c*). A section of the discretized laminate is shown, which is comprised of a stack of 16 thin shell elements of 0.123mm thickness, each representing a ply. Figure 8 provides a table specifying the laminate layup used for experiments and simulations. The residual stresses analysis is carried out at each discretized laminate level which will be discussed in the following subsection.

The temperature data of the punch and die is recorded during the cooling phase of thermoforming experiment as mentioned in Section 3.4.1. The temperature data of punch and die between 200°C and room temperature is utilized which is shown in Figure 9. The cooling period of the punch and die is 400s and 370s respectively beyond which constant room temperature is assumed. These cooling curves are input as boundary conditions to perform the transient thermal analysis. The implicit FE analysis is carried out for the total cooling simulation time, t = 660s similar to the experiment. The material properties used for this analysis are listed in Table 1. The adjacent plies of the laminate are expected to have micro voids and defects at the contact interface which may develop thermal contact resistance resulting in an increased thermal gradient. This is accounted for by defining a gap conductance of 0.1 mW/mm^2K [51]. The through thickness temperature evolution of the hat structure is determined from the transient heat transfer analysis.

The temperature data is recorded in an ASCII format which is further used in a MATLAB script to calculate the residual stresses evolution through the laminate thickness.

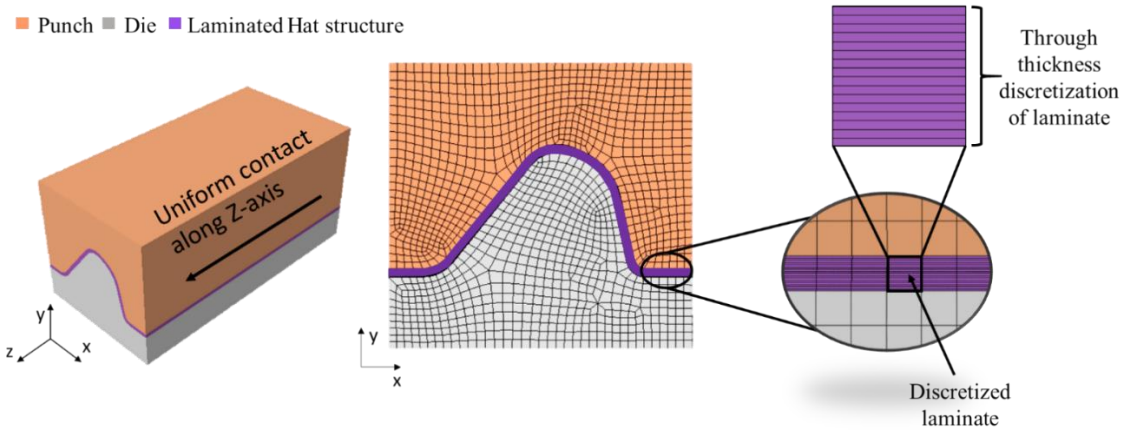

(a) *(b)* *(c)*

Figure 7 (a) Finite element 3D model setup in global coordinate system (x,y,z), (b) simplified 2D (x,y) model setup for transient heat transfer simulation (c) FE discretization of the laminated hat structure

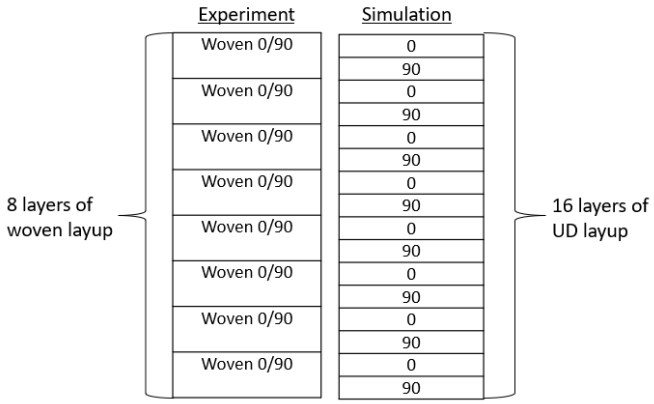

Figure 8 Laminate layup used in experiments and simulations

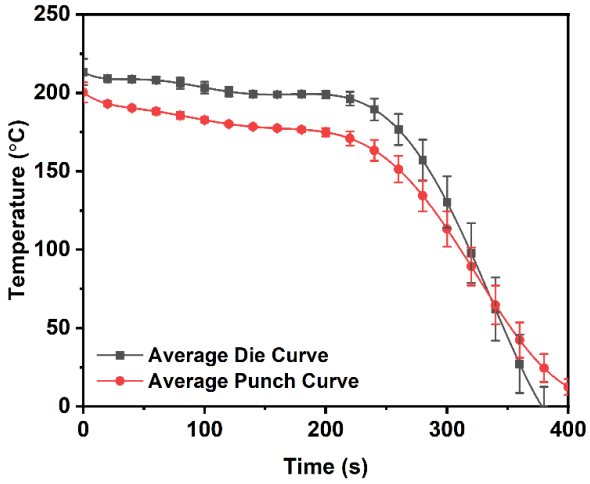

Figure 9 Cooling curves defined for Punch and Die obtained as average from 3 experimental trials. Punch has cooling rate of -0.9 °C/s between 170-60°C, -1.3 °C/s between 60°C -RT, Die has a cooling rate of -1.5 °C/s between 170-60°C, -1.8 °C/s between 60°C -RT

4.2.2 Determination of residual stresses

The residual stresses due to through thickness thermal gradient in a laminated composite structure can be determined by following the incremental classical laminate theory based thermomechanical analysis as discussed by [46,47]. According to this, the cooling process is discretized into *n* time steps and the residual stresses at ply level (incremental ply stresses) are determined at each time step. The total residual stresses at the end of cooling process for any given ply, can be calculated by taking a cumulative sum of these incremental ply stresses. This analysis is carried out by implementing FE approach using a MATLAB script. The same discretization strategy as discussed for transient heat transfer analysis is utilized herein. To explain the analysis, consider a laminate structure comprised of *16* plies, oriented at an angle (θ) w. r. t. global coordinate system (x, y, z) as shown in Figure 10(*a*). Also shown, is the laminate local coordinate system or the analysis system (x1, x2, x3), where x2 is laminate thickness direction. Figure 10(*b*) shows the arbitrarily selected *k*-th ply having thickness e_k, and the distance from laminate midplane to ply midplane is h_k. Since the analysis is done at each discretized laminate level, the following discussion is presented in the analysis system (x1, x2, x3). The thickness of the ply (x2) is considered very small as compared to in-plane (x1, x3) dimensions of a ply. Therefore, a 2D plane stress analysis is carried out, where in-plane residual stresses are developed due to thermal gradient along x2.

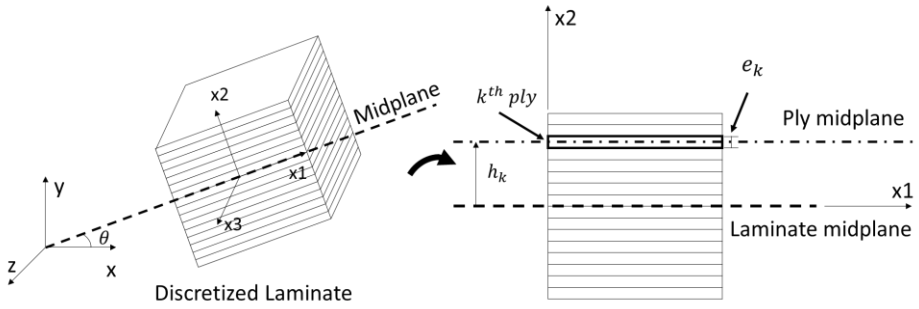

(a) *(b)*

Figure 10 Illustration of (a) a discretized laminate orientated at an angle (theta) w.r.t. global coordinate system (x,y,z). (b) k-th ply at a distance h_k from laminate midplane.

The thermoelastic constitutive equation for the k^{th} ply can be obtained in the incremental form by incorporating the incremental 'stress-free' ply strains (($\Delta\boldsymbol{\varepsilon^T}$) and laminate strains (($\Delta\boldsymbol{\varepsilon^0}$) respectively, into the Duhamel-Neumann form of Hooke's law [53]. Detailed description of the above mentioned strains are provided in Appendix B. The resulting incremental stresses in k^{th} ply is expressed as:

$$\begin{bmatrix} \Delta\sigma_{x1} \\ \Delta\sigma_{x3} \\ \Delta\sigma_{x1x3} \end{bmatrix}_k = \left[\bar{Q}_{ij}\right]_k \left(\begin{bmatrix} \Delta\varepsilon^0_{x1} \\ \Delta\varepsilon^0_{x3} \\ \Delta\varepsilon^0_{x1x3} \end{bmatrix} - \begin{bmatrix} \Delta\varepsilon^T_{x1} \\ \Delta\varepsilon^T_{x3} \\ \Delta\varepsilon^T_{x1x3} \end{bmatrix}_k \right) \tag{3}$$

where $\Delta\boldsymbol{\sigma}$ is incremental residual stresses for a ply. The residual stresses at the end of the cooling process can be obtained by taking the cumulative sum of the incremental stresses computed using Equation (3). This can be expressed for *k*-th ply as:

$$\begin{bmatrix} \sigma_{x1} \\ \sigma_{x3} \\ \sigma_{x1x3} \end{bmatrix}_k = \sum_{t=1}^{n} \begin{bmatrix} \Delta\sigma_{x1} \\ \Delta\sigma_{x3} \\ \Delta\sigma_{x1x3} \end{bmatrix}_k \tag{4}$$

The final step before mapping the residual stresses to a FE solver is to transform the ply stresses from analysis system to the global coordinate system using the transformation matrix (refer Appendix B). This is done for each ply. The global residual stresses are extracted and saved in ASCII format for each discretized laminate. The data is further used in the stress mapping code discussed in the following section. The material properties required for this analysis are listed in Table 1 and Table 2.

4.3 Mapping of numerical results

A mapping procedure is generally employed to continue analysis either in the same or different solver by transferring the results obtained from one simulation to the next. In the current study, the process-induced effects such as thickness variations, fiber reorientations, and residual stresses are mapped on a new mesh of the hat structure suitable for mechanical analysis. For the thermoforming results, the "Result Mapper" tool within the Altair Hyperworks software is used for performing the result mapping procedure. For the residual stresses, a MATLAB script is developed for the mapping.

4.4 Mechanical performance validation

The last step of the MTR pathway is to evaluate the mechanical response of the hat structure, with the process-induced effects included. In the current study, a quasi-static three-point bend test and a dynamic impact test is carried out to validate the MTR pathway. The FE analysis is carried out by using the LS-DYNA solver.

4.4.1 *Quasi-static three-point bend test*

The composite material behavior is modeled using LS-DYNA material law MAT 58 (MAT_Laminated_Composite_fabric) which models the anisotropic behavior of composite and implements the damage mechanics using the Matzenmiller-Lubliner-Taylor model [54]. More description can be found in [56]. The MAT 58 card is calibrated for the PA6 laminate by carrying out the experiments discussed in Section 3. Figure 11(a) shows the FE model setup consisting of the thermoformed composite part, a rigid impactor, and two rigid cylindrical supports of 10 mm diameter. The bottom of the thermoformed hat section is joined with a 0.5 mm flat composite spine section using an adhesive layer. The 1.97 mm thick adhesive layer has width of 10 mm on both sides of hat section which is modeled using solid cohesive elements which act like springs in through-thickness direction. The cohesive mixed mode material model [57] is used to model adhesives which follows purely elastic behavior with bilinear traction separation failure law.

4.4.2 *Dynamic impact test*

An impact test with 28.75J impact energy is simulated in LS-DYNA by striking a 3.1kg rigid cylinder to the hat structure with an impact velocity of 4.3m/s. The model setup and boundary conditions are applied such that it replicates the experiments. Figure 11(b) shows the FE model setup for impact tests where a hat structure is placed over a rigid fixture. The clamp conditions on flat edges of hat structure as described in the experiment section are simulated by applying SPC boundary conditions on the nodes constraining all

six degrees of freedom. To model composite material, the enhanced composite damage material model, MAT54 is used.

A thin shell element approach is implemented wherein the laminate layup is defined by a single integration point for every single ply consisting of respective fiber orientation and thickness. Detailed description of the failure behavior can be found in [56]. Once, the failure criteria are satisfied for all the plies, then the whole element is eroded. The nearby elements become "crashfront" elements and their strength can be reduced based on the SOFT parameter. A fully integrated shell element formulation (ELFORM =16) is used to eliminate hourglass modes and laminate shell theory is invoked by setting LAMSHT=1 in *CONTROL_SHELL. This option removes the usual assumption of uniform shear strain through the thickness of the shell which is important for sandwich composites with soft cores [56]. MAT 54 card is sensitive to mesh size, contact formulation and non-physical crashfront softening parameter SOFT-[58–62]. An optimal mesh selection approach for MAT54 card requires a trade-off between accuracy and computational time and it should also closely replicate the physical damage behavior. Therefore, in the current study a mesh size of 2mm X 2mm is used and is kept consistent throughout the MTR pathway. The LS-DYNA keyword *PART_COMPOSITE is used to define individual composite layers along with their thickness and offset angle (BETA). Figure 11(b) shows the zone-based representation of composite hat structure, where each colored zone represents LS-DYNA part composite that embodies a unique set of stack-up order of composite laminate.

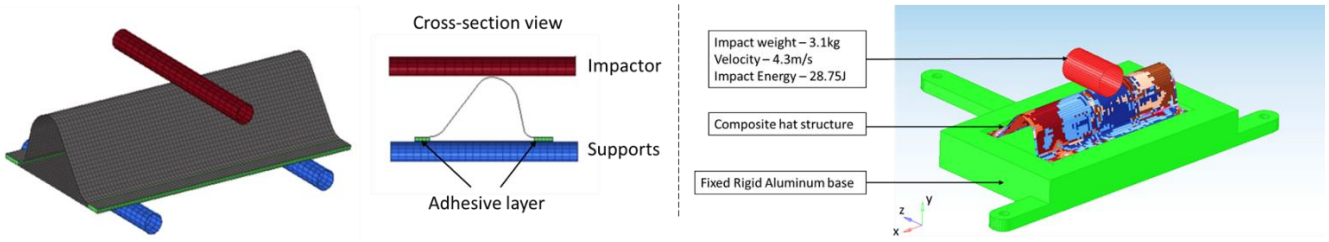

(a) *(b)*

Figure 11 (a) FE model setup for mechanical tests showing thermoformed hat structure adhesively bonded with spine along with rigid impactor and supports (b) FE model setup for impact test showing thermoformed hat structure with rigid impactor and fixed support.

4.5. Numerical study: Static and dynamic analysis

The thermoforming process may result in variations in thickness distribution, fiber orientation, and residual stresses distribution due to factors such as complex geometry, thermoforming tool clearance, and surface

finish. In this study, to demonstrate the MTR pathway, a thermoforming tool with a high surface finish is used to form a hat section structure with a relatively simple and smooth geometric shape. As a result, no large variations in thickness and fiber orientations are produced. To understand the effect of large variations in thickness and fiber orientation on the structural response under static and dynamic loading. In our numerical studies, we artificially increase the range of thickness and fiber orientation variations on the same hat section geometry. The different variations in residual stresses are obtained by carrying out the cooling analysis discussed in Section 4.2 for various cooling rates. The computational model is setup to carry out static and dynamic analysis with the inclusion of these variations. The results are obtained for several cases and compared with the response of the hat structure without considering thickness and fiber orientation variations and residual stresses.

4.5.1 Static analysis

The static test is first carried out to evaluate the overall stiffness of the hat structure. This is done by setting up six static load cases as illustrated in Figure 12 which are (a) longitudinal compression, (b) longitudinal shear, (c) longitudinal bending, (d) transverse compression, (e) transverse shear and (f) transverse bending. An implicit FE analysis to solve the linear static problem is setup in LS-DYNA. To model the composite behavior MAT 58 discussed previously is used. A force of 4 N is applied to each node of the loading edge which results into an external force of 220N for the three longitudinal load cases while a force of 304N for the three transverse load cases. The corresponding deflection is measured and compared for all the cases.

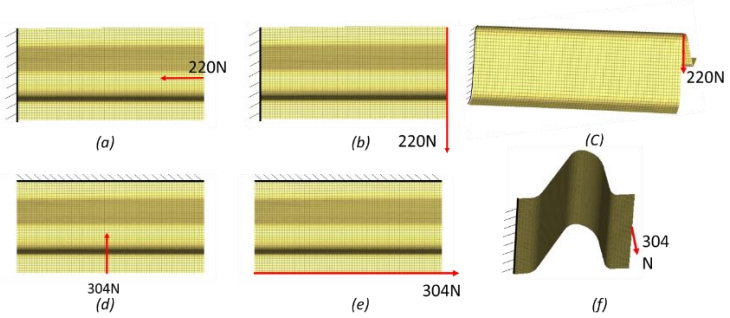

Figure 12 A schematic diagram of six static load cases representing (a) longitudinal compression, (b) longitudinal shear, (c) longitudinal bending, (d) transverse compression, (e) transverse shear and (f) transverse bending.

4.5.2 Dynamic analysis

The dynamic impact test is simulated on the thermoformed hat structure in LS-DYNA using the same modeling strategy as described earlier. However, for the purpose of the numerical study, a higher energy impact 57.5J is simulated. Further, a cylindrical impactor may result in localized deformation in the hat structure and may not give a complete picture of the various process-induced effects. Thus, a larger contact

area impact test is simulated by using a rigid plate impactor of 6.22kg and the impact velocity of 4.3m/s which is shown in Figure 13. The edges of the hat section are kept fixed while a rigid support at the bottom of the structure is placed to hat structure to collapse.

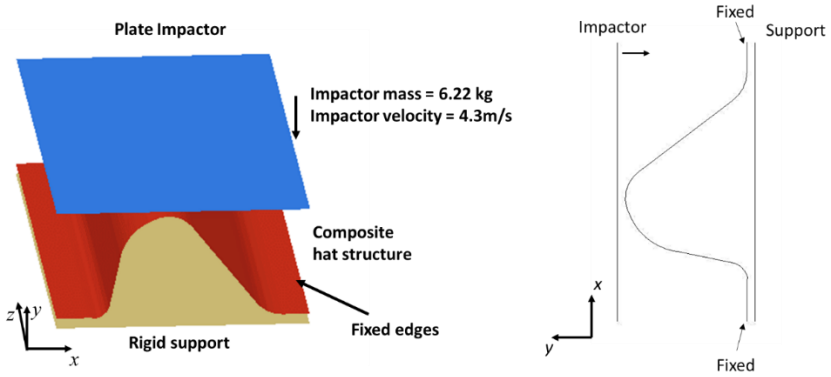

(*a*) (*b*)

Figure 13 FE model setup of the impact test showing composite hat structure with fixed edges impacted by a rigid plate (a) front view and (b) 2D cross-sectional view.

5. Results and discussion

5.1. Model validation *(Experimental vs numerical)*

The MTR pathway developed in this study is validated at two steps i.e. first at the manufacturing stage which is followed by the mechanical testing stage. At the manufacturing stage, thickness variations and fiber reorientations are validated at the structure level. At the mechanical testing stage, the combined effect of residual stresses, thickness variations, and fiber reorientations on the structural response is validated with the experiments.

5.1.1 Thermoforming results: Thickness variation and Fiber Orientations

The thickness variation and fiber orientations are experimentally measured after performing the thermoforming experiments and are compared with the numerical results. The thickness is measured at six different locations along the hat profile (or three locations on each side) and the average thickness from the three experimental trials is presented in Figure 14. The maximum thickness of 2.01mm is observed at location 5 with the standard deviation of 0.008mm, while the minimum thickness of 1.97mm is observed along the flatter edges locations 1 and 3 with the standard deviation of 0.01mm. Figure 14 also presents the numerically predicted thickness contour (uniform along z-axis) along the two sides of the hat structure. The numerical thickness variation is predicted using the draping tool of Altair Hyperworks. A comparison between the measured thickness and the predicted thickness shows good agreement. Further, the warp and weft tows of the composite sheet are referred here as fibers in directions 1 and 2 initially 90° apart. These

fibers of the composite sheet undergo reorientation as the sheet deforms to take the shape of the mold. Figure 15 shows a comparison of fiber orientations obtained from the experiments and simulation, where the change in angle between the two fiber directions is measured. On the fabricated hat structure, four locations are identified (highlighted square in Figure 15) to capture fiber orientations at different geometric curvatures of the hat structure. To compare with the numerical results, a closer view of these locations is shown in Figure 15 along with the numerically obtained contour plot of fiber orientations at the four specified locations. The maximum fiber angle of 103° can be observed from the contour plot near location 4, which means a fiber reorientation of 13°. The average fiber orientations from the three experimental trials are determined and compared with the numerical prediction. The comparison shows good agreement with a maximum difference of 3.3%. Note that both the thickness variations and fiber orientations need to be mapped to the hat structure before mechanical validation.

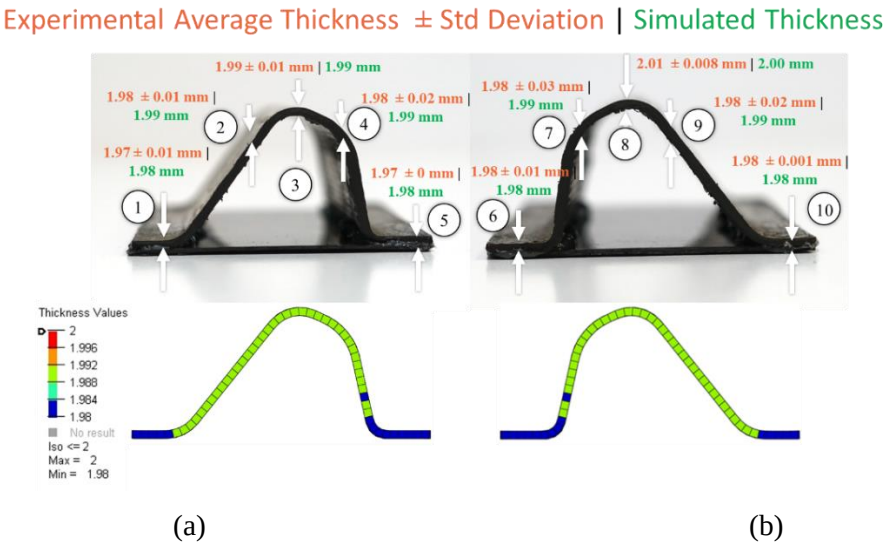

Figure 14 Thickness variation in the hat structure: (a) Side 1, (b) Side 2 represented as (upper) measured average thickness ± standard deviation and (lower) predicted thickness variation (uniform along z-direction).

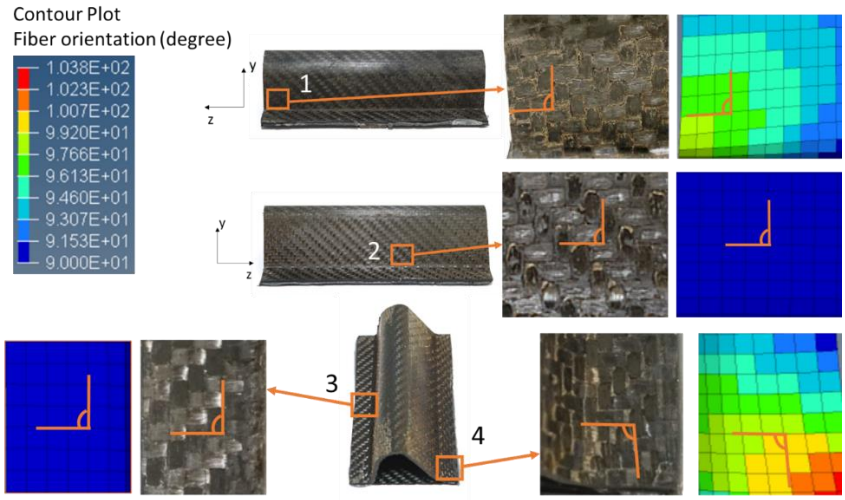

Figure 15 Fiber orientation in degree as observed in thermoforming trials and simulation at marked locations of the hat structure

5.1.2 Residual stresses: validation and results

The residual stress model described in Section 4.2.2 is implemented for APC-2 composite laminates to validate the residual stress calculation procedure with prediction results reported by Chapman et al. [46]. The laminate consists of 40 unidirectional APC-2 sheets amounting to a total thickness of 5 mm. The temperature evolution data through the laminate thickness and cooling curve reported in [46] are used as input. Residual stresses evolution in the transverse direction (perpendicular to the fiber direction) for surface and center plies is reported in the paper and used for comparison with this work as shown in Figure 16(*a*). Furthermore, the distribution of transverse residual stresses through the laminate thickness at t = 60 sec is compared with the predicted results for an initial cooling rate of 35°C/s as shown in Figure 16(*b*). It is important to note that a curve is fit through the data points obtained in this work for Figure 16(*b*). It is shown that the results obtained from the residual stresses model compare reasonably well with the model prediction data from [46]. The discrepancy in results can be attributed to the fact that the effect of degree of crystallinity on the material properties is not considered in the residual stresses model here.

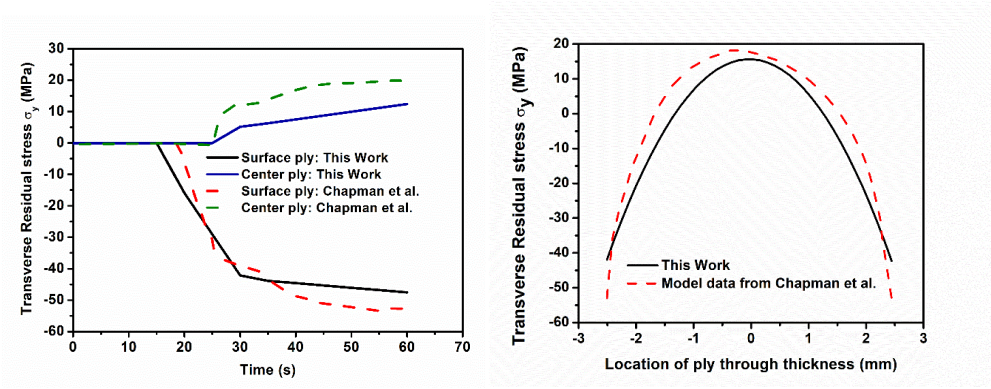

(a) *(b)*

Figure 16 Validation of Residual stresses code with model prediction data from Chapman et al. [46] (a) Comparison of transverse residual stresses σ_y evolution for surface and center plies, (b)comparison of transverse residual stresses σ_y distribution through the laminate thickness at t = 60 sec

To illustrate the residual stresses evolution, consider a discretized laminate as shown in Figure 17(*a*). This laminate is oriented at an angle (θ = 19.2°) w. r. t. global coordinate system (x, y, z). As seen in Figure 9, the punch and die have different cooling rates. As a result, the ply immediately in contact with the die (SD) and the ply in contact with the punch (SP) cool in dissimilar manner. Consequently, an asymmetric stress profile along the thickness of the laminate is obtained where higher compressive stresses are developed in SP as compared to SD in this particular case. This asymmetry can be observed in Figure 17(*b*), where residual stresses ($\sigma_z, \sigma_x, \sigma_y, \sigma_{xy}$) are plotted against the location of ply (*h*) through thickness, where *h* ranges from -1 to 1. These stresses are according to Equation (8) in Section 4.2.2. Tensile stresses are observed towards the center ply (*h* = 0) while compressive stresses are observed going from the center towards the two surface plies at *h* = +1 and *h* = -1. The magnitude of residual stresses observed in $\sigma_z, \sigma_x, \sigma_y, \sigma_{xy}$ in Figure 17(*b*) at the center ply *h* = 0 and at two surface plies at *h* = +1 and *h* = -1 are tabulated in Table 3. The incremental residual stresses (σ_z) evolution during simulation time, *t* = 660 s, is presented for center and surface plies SD and SP in Figure 17(*c*). As mentioned earlier, the residual stresses buildup starts once all plies in the laminated hat structure reaches *Tc* (=170 °C) of PA6 matrix.

The residual stresses calculated incrementally are directly proportional to ($\Delta\boldsymbol{\varepsilon^0} - \Delta\boldsymbol{\varepsilon^T}$) from Equation (3). The stress-free strains $\Delta\boldsymbol{\varepsilon^T}$ are in turn dependent on the cooling increment ΔT. In the initial phase of cooling, the rate of cooling of the surface plies is much higher than the center plies. This results in an overall lower laminate midplane strain $\Delta\boldsymbol{\varepsilon^0}$. The difference ($\Delta\boldsymbol{\varepsilon^0} - \Delta\boldsymbol{\varepsilon^T}$) then generates incremental tensile stress near the surface whereas compressive stresses towards the center of the laminate. However, as the cooling progresses, the rate of cooling of the center plies increases until a threshold value of $\Delta\boldsymbol{\varepsilon^0}$ is reached. Beyond this stage, stress reversal is observed eventually leading to compressive stresses in surface plies and tensile

stresses towards the center. This can be better understood by studying the ΔT over the cooling period (see Figure 17(d)). In the initial cooling period from approximately 200 - 368 sec, ΔT for SD and SP plies is higher than the center ply. Correspondingly, incremental tensile stresses are observed in SD and SP plies whereas compressive stresses are observed in center ply in Figure 17(c). Beyond 368 sec, ΔT in center ply is higher than the center plies till the end of cooling. This translates into stress reversal in Figure 17(c). The residual stresses are mapped on the hat structure for each discretized laminate to carry out the mechanical tests. Figure 18 shows the contour plot of residual stresses (σ_z) distribution on the center and surface plies SD and SP, for the 3D laminated hat structure. Recall that a uniform contact along the z-axis of the hat profile is assumed during the heat transfer analysis. As a result, the residual stresses magnitude along z-axis for each discretized laminate is uniform as seen in Figure 18.

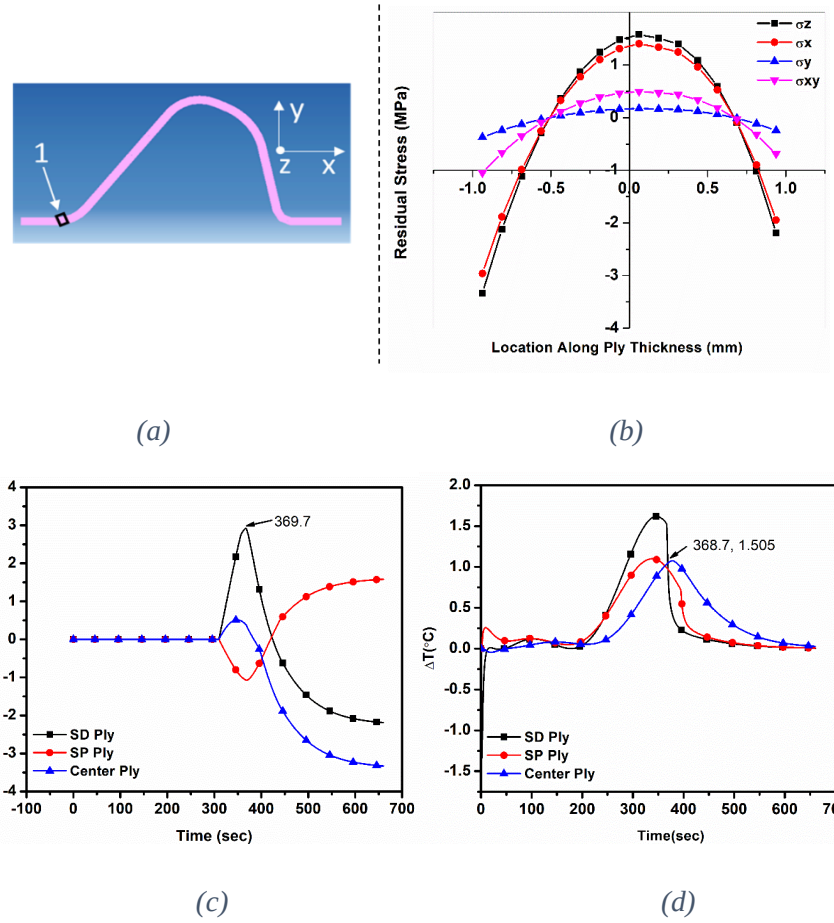

Figure 17 (a) A discretized laminate considered from the hat structure, (b) residual stresses ($\sigma_z, \sigma_x, \sigma_y, \sigma_{xy}$) against the location of ply (h) through thickness, where h ranges from -1 to 1, (c) evolution of residual stresses (σ_z) in surface plies S1, S2 and center ply through t = 660s, (d) cooling increment (ΔT) vs time in the surface plies SD,SP and center ply.

Table 3 Magnitude of residual stresses (σ_z,σ_x,σ_y,σ_xy) at Surface, h = ±1 and center, h = 0 plies

Residual stress (MPa)	σ_z	σ_x	σ_y	σ_{xy}
Center, h = 0	**1.48**	**1.31**	**0.16**	**0.46**
Surface, h = +1	**-2.18**	**-1.94**	**-0.24**	**-0.68**
Surface, h = -1	**-3.33**	**-2.95**	**-0.36**	**-1.04**

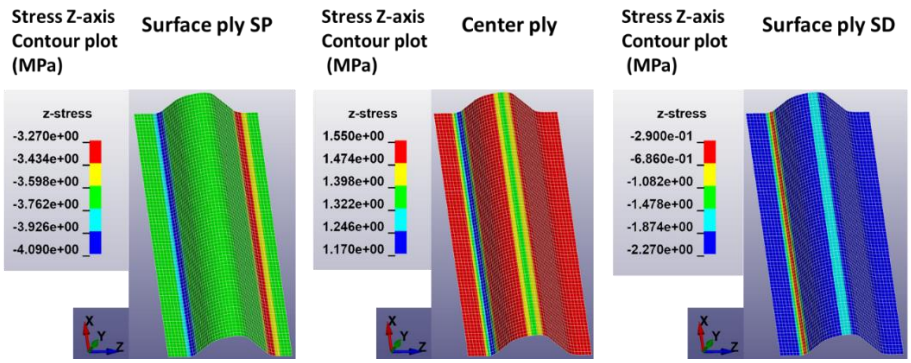

Figure 18 Contour plot showing residual stresses distribution along Z-axis on center and surface plies SP and SD of the laminated hat structure.

5.1.3 Mechanical performance validation

Quasi-static test validation

The experimental and numerical performance of thermoformed hat structure under quasi-static 3-point bending test is presented here. The force vs displacement plot is compared in Figure 19 and the damage behavior is presented in Figure 20. Figure 19(*a*) presents the force vs displacement plot of the three experimental trials. It can be observed that all three trials show a consistent and repeatable linear stiffness zone. The three trials also show consistent failure initiation at approximately 6 mm deflection across all samples. Additionally, the location, time, and displacement at which crack initiation occurs is very consistent across 3 samples as shown in Figure 20(*a*). The trials do show a slightly varied force-displacement response post 7 mm deflection with trial one exhibiting a peak load of ~ 5877 N at 10 mm deflection while trial 2 and trial 3 show loads around 5272 N and 4652 N, respectively, at the same deflection. The final shape and deflection of the crack vary slightly across the three samples with trial 1 showing the least damage in terms of crack diameter and deflection and trial 3 showing the most damage. The numerical 3-point bend test under quasi-static loading conditions is carried out using LS-DYNA after mapping the thermoforming effects. The force-displacement response is compared with the mean experimental results in Figure 19(*b),* which show a very good agreement till damage onset. The large deformation is observed at the impact location of the hat structure and the numerical damage prediction is compared with the three experimental trials as shown in Figure 20(*a*). It is observed that numerical

prediction of deformation closely matches trial 3. Figure 20(*b)* presents the top view of the hat structure along with Von-Mises stress contour and the encircled regions (in red) show damaged locations. The damage behavior is consistent with the experimental results. However, it should be noted that delamination failure and damage propagation which requires a detailed damage modeling strategy are not considered in the study.

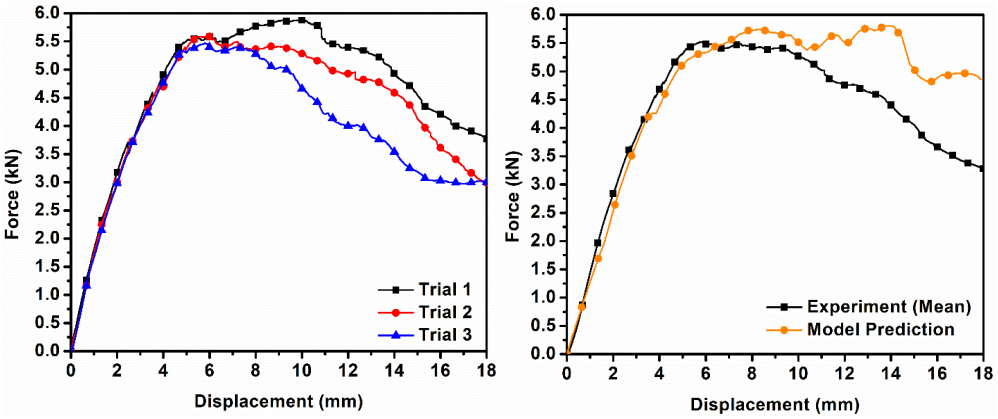

(a) *(b)*

Figure 19 (a) Force-displacement plot of three experimental trials (b) force-displacement plot for 3-point bend test comparing the experimental response with numerical prediction.

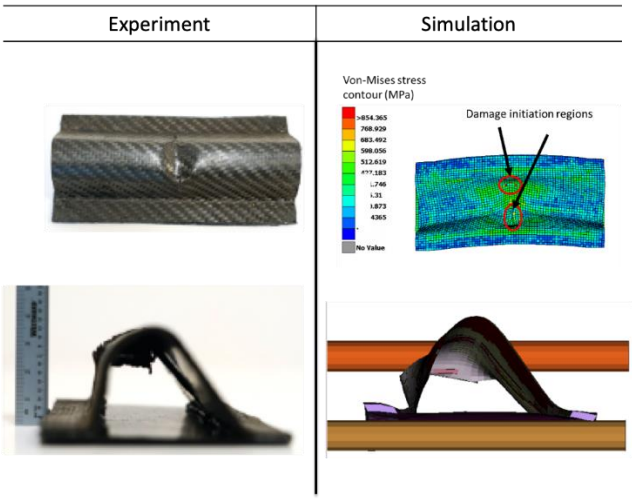

(a) *(b)*

Figure 20 Deformation comparison between experimental trials and numerical simulations (a) deformation side view: close match with experimental trial 3 and (b) top view comparison with stress contour plot. Encircled are the damage initiation locations on the structure.

Dynamic impact test validation

The experimental and numerical performance of hat structure under dynamic impact test is discussed here. The dynamic performance is evaluated by plotting a force vs time curve which gives the crush stiffness and peak crush resistance force for the studied impact. The force vs time plot of the three experimental trials is shown in Figure 21(*a*) where, the highlighted red arrows indicate the crush force at three locations i.e. at initial impactor contact, at maximum impactor stroke, and when the impactor finally losses contact with the hat structure. In Figure 21(*b*), front view of the three experimental trials is presented which shows the impactor position for the three corresponding locations. It is observed that a maximum stroke of 6.9mm, 7.3mm and 7.2mm is obtained for the three trials (mean experiment maximum stroke = 7.1mm). The experiments show a consistent and repeatable performance in terms of crush stiffness (linear slope), peak crush force and integral (area under the curve). To validate the MTR pathway, the mean experimental performance is compared with the numerical response of the hat structure under the dynamic impact test. A force vs time response plot is presented in Figure 22(*a*). A reasonable correlation is observed between the two curves, where the peak mean experimental force is 5.3kN while the peak numerical force is obtained as 4.5kN. Further, the experimental damage that occurred in the hat structure is compared with the numerical predictions in Figure 22(*b*). The encircled region shows the locations of the damage which is similar for both experiment and simulation. A von-Mises stress contour plot is also presented in Figure 22(*b*) at the maximum impactor stroke which shows the stress distribution is highest at the vicinity of impact. The maximum impactor stroke of 7.35mm is obtained from the simulation which is very close to the mean experiment maximum stroke. Table 4 presents the peak force and integral value (area under the curve of the force-time plot) for both experiment and numerical dynamic impact test. The integral value indicates the impactor kinetic energy absorbed by the hat structure during the test. It can be observed that the mean experimental integral value is 1681 N-ms which is close to the numerically predicted integral value of 1639 N-ms.

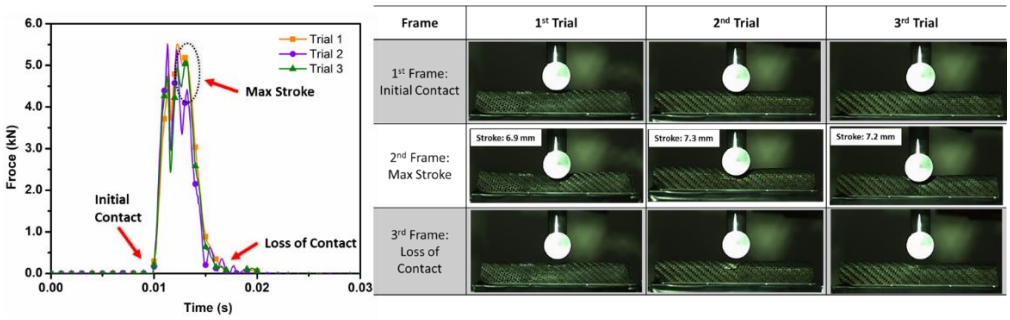

(*a*) (*b*)

Figure 21 Dynamic impact test performance:(a) Force vs time plot showing three experimental trials and (b) front view of the experimental trials showing impactor position at initial contact, at maximum stroke and at loss of contact.

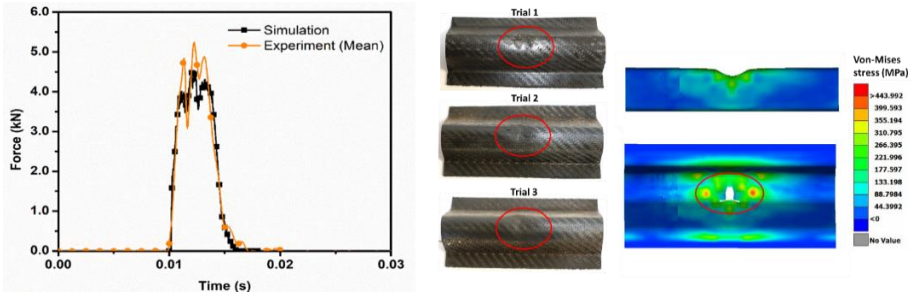

(*a*) (*b*)

Figure 22 (a) Validation of dynamic impact test: Force vs time plot comparing experiment and simulation. (b) damage comparison of the experimental trials and numerical prediction.

Table 4 Dynamic impact test comparing experiment and numerical performance

Dynamic impact test	**Peak Force (N)**	**Integral (N-ms)**
Experiment trial 1	5515	1791
Experiment trial 2	5513	1593
Experiment trial 3	5107	1661
Mean (Standard deviation)	5378 (235)	1681 (100)
Numerical simulation	4545	1639

5.2. Numerical study: manufacturing process effects on static and dynamic response

5.2.1 Thickness variation

In an ideal scenario, the hat structure has a uniform thickness of 2 mm with no variation (unmapped case). However, during the processing stage, several factors such as a non-uniform tool gap, depth-to-width ratio

of the thermoforming tool, and thermoplastic flow characteristics at high temperature may affect the final thickness distribution in the hat structure. Consequently, two cases are considered here, with 1% (T01) and 3% (T03) variation in thickness from the ideal thickness of 2 mm. The thickness distribution obtained from the MTR pathway is multiplied by a constant factor such that the difference between maximum to minimum thickness is 1% and 3% respectively for T01 and T03. The maximum thickness is kept constant as 2mm. The static responses for the six static load cases are presented in Table 5. It is seen that the static deflection increases with an increase in thickness variation for all load cases. The thickness variation changes the material volume which affects the static stiffness.

Table 5 Static performance: effects of variation in thickness distribution

			Deflection (mm)			%Change	
S No	**Load Cases**	**Force (N)**	**Unmapped**	**T01**	**T03**	**T01**	**T03**
A	Longitudinal Compression	220	0.0027	0.0027	0.0028	1.06%	5.36%
B	Longitudinal Shear	220	1.6752	1.6982	1.7905	1.37%	6.88%
C	Longitudinal Bending	220	0.3356	0.3400	0.3581	1.33%	6.71%
D	Transverse Compression	304	1.7453	1.8011	2.0372	3.20%	16.73%
E	Transverse Shear	304	1.8988	1.9585	2.2107	3.14%	16.43%
F	Transverse Bending	304	9.7700	10.0841	11.4114	3.21%	16.80%

Next, the impact performance is evaluated for the two thickness variations and the force-displacement curves of the impact load cases are shown in Figure 23. Note that the area under each curve gives the kinetic energy absorbed during the impact. It is shown that each curve forms a closed-loop after reaching maximum displacement, which represents the rebound of the impactor from the hat structure. To understand the force-displacement plot, the progressive deformation of hat structure from t = 0 to 10ms is presented for both unmapped and T03 case in Figure 24. Consider the unmapped case of uniform thickness, as the deformation progresses from t = 0ms to t = 1ms, both the longer and shorter edges of the hat structure undergo compression during which the maximum peak force of 12kN is attained. The compressive failure occurs along the bend region of the shorter edge which results in flattening of the top of the hat structure and thereby increases the contact area between the impactor and hat. The failure is explained further in the next subsection. At t = 4ms the impactor displacement is 9.61mm, the part of the structure corresponding to the longer edge undergoes a snap-through to reach another stable configuration as shown in Figure 24, resulting in the reduced contact area. At t = 6ms, the impactor continues to push further the shorter edge of the hat structure over a smaller contact area till all the impactor energy is absorbed. The maximum impactor displacement of 11.44mm is reached for the unmapped case at t = 6.6ms beyond which the impactor rebounds due to the spring-back effect. This effect can also be observed in the force vs displacement plot

in Figure 23, where force increases to a higher value before the rebound. Since the thickness variation results in material volume change which is directly related to the material stiffness and strength and therefore a slight variation may affect the response significantly. It is observed as the thickness variation is increased (the average thickness is reduced), the initial slope of the curve which represents the initial crush stiffness reduces. Further, the compressive failure in the shorter edge occurs earlier than the unmapped case resulting in the drop in the peak force to 11.7kN and 11.3kN for T01 and T03, respectively. On comparing the progressive deformation of unmapped and T03 cases in Figure 24 it can be observed that at any given time t < 6ms, the impactor displacement is higher for T03 than unmapped case due to overall reduced strength of the structure and early failure. At t = 6ms, a higher snap through effect can be observed for T03 and the maximum impactor displacement of 12.05mm is obtained at t = 6.4ms. Due to this larger impactor displacement or larger pushing of the hat structure, a higher spring back force of 6.5kN is affected.

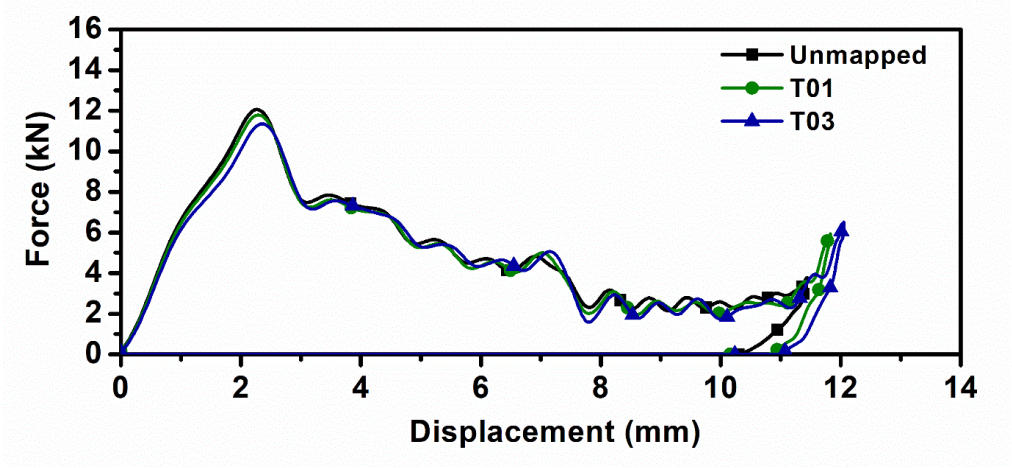

Figure 23 Force vs displacement plot under impact loading comparing two cases of thickness variation with unmapped case.

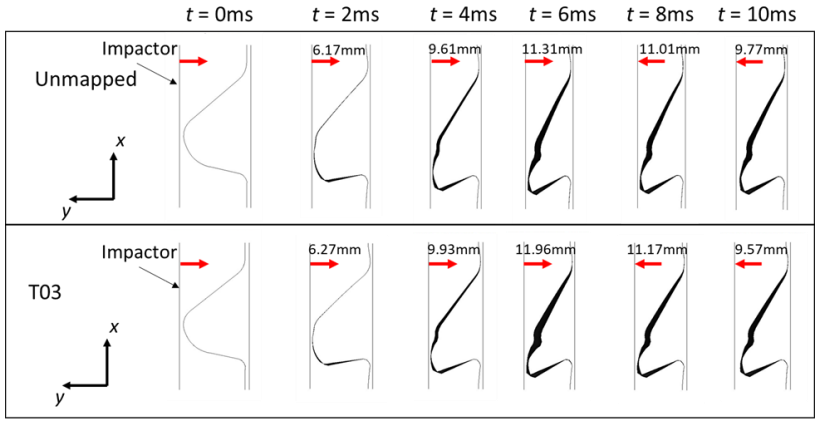

Figure 24 Progressive deformation of hat structure under impact loading showing the effect of thickness variation.

5.2.2 Fiber orientations variation

Thermoforming a component with complex geometry can lead to large variations in fiber orientation over the formed component. For the numerical analysis in this section, two different fiber orientation variations are generated and compared with the original 0/90 configuration (unmapped case). This is done by multiplying the shear angles obtained from the actual thermoforming result of the hat structure by a constant factor. The two cases are D20 with a maximum shear angle of 20 degrees and D35 with a maximum shear angle of 35 degrees. The fiber orientation distributions for the three cases are shown in Figure 25.

The numerical tests are carried out first for the six static load cases and the responses are presented in Table 6 and a comparison is made with unmapped configuration. With an increase in shear angle, the stiffness under longitudinal compression, transverse compression, and bending is reduced. Under longitudinal shear and bending and transverse shear loads the structural stiffness is reverse for the two cases D20 and D35. This is mainly due to the nonsymmetrical cross-section of the hat structure which results in a higher cumulative nodal force distribution on the longer side. Due to this a pure bending or shear test is not simulated, and instead, an additional twist is added to the structure, thereby changing the line of action of the resultant force. The configuration with fibers orientated along the line of action would give maximum stiffness, which here is observed for the D20 case. To further confirm the observation, more fiber orientation variations between 0 and 40 degrees are simulated. It is found that there is an optimal fiber orientation configuration that gives the maximum stiffness for each load case (results are not presented here).

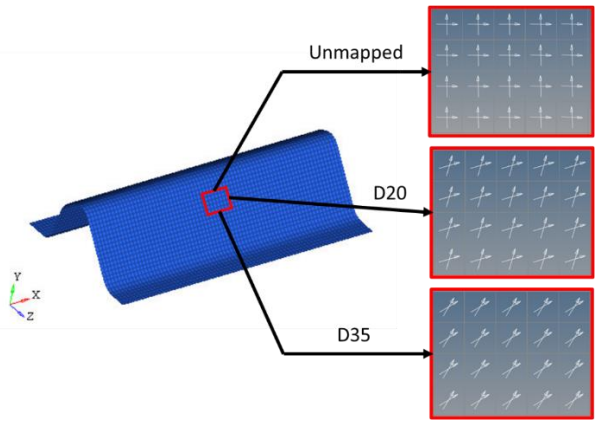

Figure 25 Fiber orientations for the three cases unmapped, D20 and D35.

Table 6 Static performance for the two orientation variants

S No	Load Cases	Force (N)	Deflection			%Change	
			Unmapped	D20	D35	D20	D35
A	Longitudinal Compression	220	0.0027	0.0031	0.0059	14.3%	118.3%
B	Longitudinal Shear	220	1.6752	1.5796	2.0472	-5.7%	22.2%
C	Longitudinal Bending	220	0.3356	0.2703	0.4158	-19.5%	23.9%
D	Transverse Compression	304	1.7453	1.9869	2.7002	13.8%	54.7%
E	Transverse Shear	304	1.8988	1.5629	1.4130	-17.7%	-25.6%
F	Transverse Bending	304	9.7700	11.2838	15.4205	15.5%	57.8%

Next, the effect of fiber orientation variation on crash performance is evaluated. The force-displacement results for all three cases are plotted in Figure 26. It is found that the initial stiffness of the unmapped case is higher than the D20 and D35 cases, whereas the peak force is maximum for D35 case as 14.9kN while for D20 it is 12.2kN, a little higher than unmapped case. The progressive deformation of hat structure for the unmapped and D35 cases is presented in Figure 27 for the simulation time from $t = 0$ to 1ms. From the simulation time $t = 0$ to 0.5ms, as the impactor pushes the hat structure over a small contact area, the flanges of the hat structure rest on the fixed support, while a localized in-plane deformation occurs in the vicinity of impactor contact, where the impactor flattens the curved hat top profile increasing the contact area. Now, consider a single-ply consisting of two fiber tows. For the unmapped configuration, the two fiber tows are 90 degrees apart (see Figure 25) as a result the maximum resistance to an arbitrary in-plane force can only be equal to the maximum strength of a single fiber tow, whereas for D35 both fiber tows form an acute angle (35 degrees) (see Figure 25). Therefore, the maximum resistance can be equal to maximum resultant strength to two fiber tows (which is higher than the resultant strength of 90-degree configuration). Similarly, for the unmapped fiber configuration (0/90) the minimum resistance to an arbitrary in-plane force is higher than that of the D35 case. Thus, the average in-plane strength is higher for unmapped configuration as compared to D35. Therefore, the unmapped case gives higher resistance to in-plane deformation at impact vicinity for $t < 0.5$ms. As the impactor pushes further, both sides of the hat structure undergo compression. Due to the non-symmetrical structure, the shorter side (also steeper) experiences larger compressive force than the longer side. The line of action of this compressive force is along the vertical tow direction (see Figure 25). As a result, for the unmapped case at $t = 1$ms, compressive failure occurs at the bend of the shorter edge (see encircled region for unmapped case in Figure 27). However, for the D35 case, the shorter edge is more resistant to failure as both fiber tows are along the line of action. Therefore, as the impactor pushes further, the longer edge undergoes out of plane bending (as the encircled region for the D35 case in Figure 27) while absorbing more energy. This explains the difference between peak forces for the two cases in Figure 26. The von-mises stress contour plot (top view of hat structure) is also presented at $t = 1$ms comparing both unmapped and D35 cases. It can be observed that significantly higher stresses are present

along the longer edge for the D35 case as compared to the unmapped case. As the deformation progresses, the impact occurs over a much larger contact area for D35 than in the unmapped case resulting in much quicker energy absorption for the D35 case. This shows that both static and dynamic performance is highly sensitive to fiber orientations since the material strength and modulus are directly dependent on them.

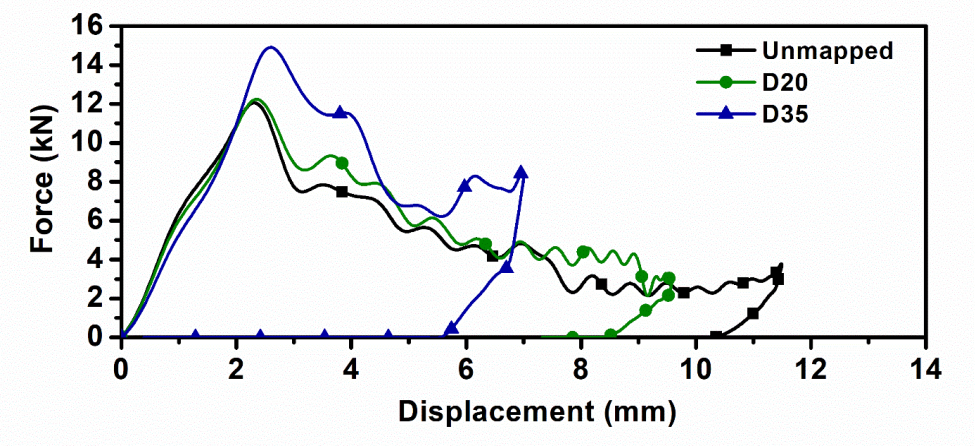

Figure 26 Force vs displacement plot comparing impact performance for the two fiber orientation cases

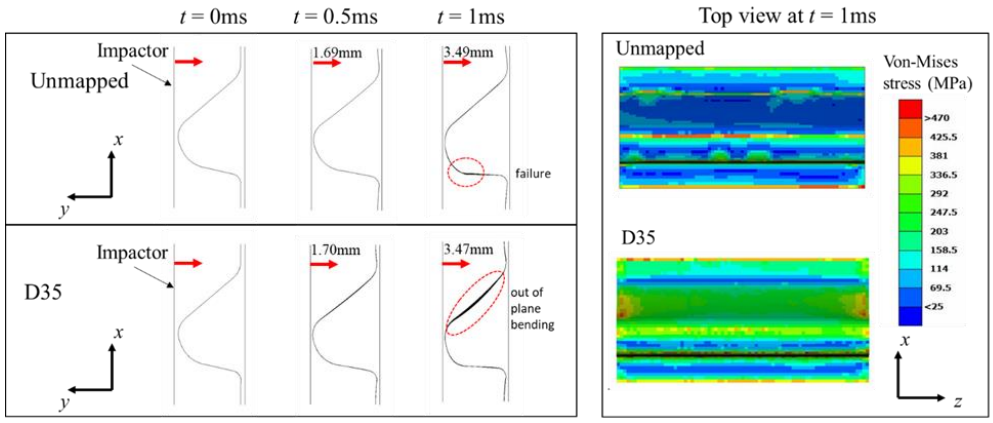

Figure 27 Unmapped vs D35: initial deformation of hat structure under impact loading and von-mises contour plot at time t = 1ms.

5.2.3 Cooling rate variation

While large-scale production of a thermoformed composite structure requires faster cooling cycles, higher cooling rates can induce undesirable residual stresses as discussed earlier. The effects of change in cooling rate on static and dynamic performance are discussed here. For comparison, residual stresses are calculated for two cooling rates 25 ºC/s (case CR25) and 30 ºC/s (case CR30). These stresses are then mapped to a new mesh of the hat structure for evaluation of the static and impact performance. The average von-Mises stress contour plot on hat structure is presented in Figure 28. Maximum stress of 21MPa is obtained for

CR25 and 26MPa for CR30. The results for three cases are compared to the case without cooling rate effect (unmapped case). From static analysis, it is observed that there is no significant change in stiffness for longitudinal shear, bending, transverse compression, shear and bending load cases. The longitudinal compression stiffness however significantly reduced as the cooling rate is increased from 25 to 30 ^{o}C/s. The change in deflection for CR25 was predicted to be 3.7% whereas for CR30 it was predicted to be 13.1% from the unmapped case. This can be understood by fact that the hat structure is already pre-stressed along the longitudinal direction with compressive residual stresses and since the direction of loading is in the same compressive direction therefore higher deflection (or lower stiffness) is observed.

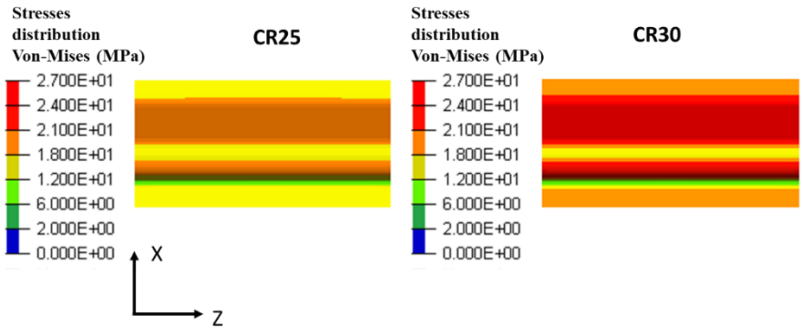

Figure 28 Von Mises residual stresses contour plot for the two cooling rate cases.

Next, the impact performance is evaluated and the force-displacement plot for various cooling rate cases is presented in Figure 29. It is observed that the initial stiffness is similar for all the cases however peak force drops with a higher cooling rate. As described earlier, both the longer and shorter edges of the hat structure undergo compression during t = 0 to 2ms and compressive failure occurs at the shorter edge for the unmapped case at t = 1ms. Now, with the introduction of compressive residual stresses in the hat structure for the CR30 case, this compressive failure in the short edge is reached a little earlier at t < 1ms resulting in a lower peak force than the unmapped case. Thus, the hat structure collapses earlier for CR30 case leading to a higher impactor displacement and larger rebound than the unmapped case.

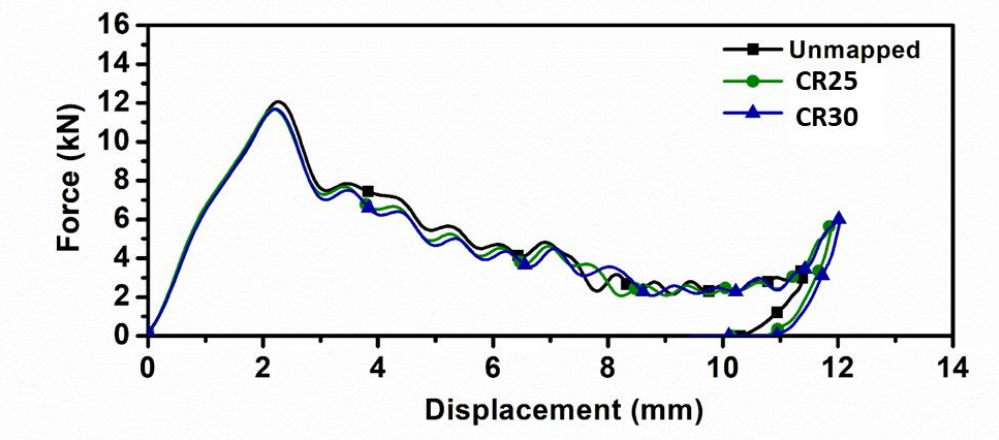

Figure 29 Force vs displacement plot showing impact performance for various cooling rate cases.

6. Conclusion

The MTR pathway is established in this study for a carbon fiber reinforced thermoplastic composite hat structure. The pathway consists of six steps: (a) material characterization and modeling, (b) thermoforming simulation with experimental validation, (c) cooling simulation, (d) residual stresses determination, (e) mapping of thermoforming effects such as fiber orientations, thickness variations, and residual stresses and (f) mechanical performance evaluation. The pathway meets the critical requirements of integrating the design and manufacturing of lightweight thermoplastic composite parts by directly linking the manufacturing process effects to the mechanical responses. The thermoforming simulations and mechanical performance are experimentally validated by first fabricating a 2 mm thick composite hat structure using thermoforming process and then performing a 3-point bend test as well as a dynamic impact test. Appropriate apparatus is developed for holding the blank in place during forming and cooling the closed mold post forming ensuring repeatability and reliability. The change in fiber orientations and thickness distribution is compared and numerical results were found to be consistent with experimental observations. To validate the residual stresses owing to cooling of the closed tool, a 3-point bend test and a dynamic impact test is simulated and compared with experiments. The experimental and simulation results namely initial stiffness and peak crush force are consistent in case of the bend test. For the dynamic impact test as well, the predicted maximum impactor stroke and absorbed impactor kinetic energy values are consistent with the experiments.

Further, the effects of the large variations in the thermoforming process-induced factors such as residual stresses, change in fiber orientations, and thickness distribution are studied numerically. The static and dynamic performance is evaluated for different cases which are summarized as:

(a) The change in thickness distribution may result in a significant reduction in static stiffness of the structure. The largest variation is observed under transverse compression load where a 16% reduction is observed for the T03 case. The impact performance also varies with thickness variation and primarily affects the dynamic stiffness and strength of the structure.

(b) The two cases of fiber orientations with large shear angle variations are studied which showed significantly higher variations in the static and dynamic performance. The largest variation is observed for longitudinal compression at the maximum shear angle of 35 degrees. It is also observed that under mixed loading conditions there is an optimal fiber orientation configuration that could give the maximum structural stiffness. The high shear angles D20 and D35 showed 18-36% increased dynamic stiffness under the studied impact load case with a much larger rebound effect.

(c) The effect of cooling rate is observed by determining the residual stresses at two different cooling rates 5 and 50C/s. These stresses are then included in the mechanical performance evaluation. Under the static loading largely, no significant change in stiffness of the structure is observed with the change in cooling rate, except, the longitudinal stiffness which is reduced significantly upon an increase in cooling rate. The dynamic performance under study deteriorated for the high cooling rate cases as early compressive failure is observed due to induced compressive stresses.

Further improvements can be made to the MTR pathway based on the current limitations. First, the pathway can be fully automated for the process steps in order to conduct manufacturing and design optimization. Second, the accuracy of the residual stresses calculation in the visco-elastic domain can be imroved by implementing an appropriate constitutive law. Third, the cumulative residual stresses developed in the structure due to micro-level, macro-level and global effects can be incorporated and validated with residual stresses determination experiments. Additionally, for complex structures, material characterization can be carried out at coupon level for manufacturing simulations and further on the component level for mechanical analysis. The scope of the current work is enormous and improvement at each step is acknowledged.

Acknowledgements

The authors are thankful for the financial support from the Department of Energy, Project # DE-EE0007293". The authors would like to acknowledge the financial support by Robert Patrick Jenkins Professorship, and Dean's Faculty Fellow Professorship. The authors are grateful to Kimberly Ivey for her assistance in conducting TMA tests and Truman Nicholson for manufacturing forming tools.

References

[1] Pradeep SA, Iyer RK, Kazan H, Pilla S. Automotive Applications of Plastics: Past, Present and Future. In: Kutz M, editor. Appl. Plast. Eng. Handb. Process. Mater. Appl. 2nd ed., Oxford: Elsevier; 2017, p. 651–74.

[2] Chiu IL, Kolb JR, Newey HA. EPOXY RESIN SYSTEM FOR COMPOSITE FLYWHEELS. Compos Technol Rev 1983.

[3] Carello M, Airale AG. Composite suspension arm optimization for the city vehicle XAM 2.0. Adv Struct Mater 2014. https://doi.org/10.1007/978-3-319-07383-5_18.

[4] Kim DH, Choi DH, Kim HS. Design optimization of a carbon fiber reinforced composite automotive lower arm. Compos Part B Eng 2014;58:400–7. https://doi.org/10.1016/j.compositesb.2013.10.067.

[5] Zhu G, Wang Z, Cheng A, Li G. Design optimisation of composite bumper beam with variable cross-sections for automotive vehicle. Int J Crashworthiness 2017;22:365–76. https://doi.org/10.1080/13588265.2016.1267552.

[6] Thakur VK, Thakur MK, Kessler MR, editors. Handbook of Composites from Renewable Materials. Hoboken, NJ, USA: John Wiley & Sons, Inc.; 2017. https://doi.org/10.1002/9781119441632.

[7] Yao S-S, Jin F-L, Rhee KY, Hui D, Park S-J. Recent advances in carbon-fiber-reinforced thermoplastic composites: A review. Compos Part B Eng 2018;142:241–50. https://doi.org/10.1016/J.COMPOSITESB.2017.12.007.

[8] Kothari A, Yerra A, Limaye M, Pradeep SA, Dalal G, Li G, et al. A Finite Element Design Study and Performance Evaluation of an Ultra-Lightweight Carbon Fiber Reinforced Thermoplastic Composites Vehicle Door Assembly. SAE Tech. Pap., 2020. https://doi.org/10.4271/2020-01-0203.

[9] EL-Dessouky HM, Lawrence CA. Ultra-lightweight carbon fibre/thermoplastic composite material using spread tow technology. Compos Part B Eng 2013;50:91–7. https://doi.org/10.1016/J.COMPOSITESB.2013.01.026.

[10] Kim DH, Kim HG, Kim HS. Design optimization and manufacture of hybrid glass/carbon fiber reinforced composite bumper beam for automobile vehicle. Compos Struct 2015. https://doi.org/10.1016/j.compstruct.2015.06.028.

[11] Liu Z, Lu J, Zhu P. Lightweight design of automotive composite bumper system using modified particle swarm optimizer. Compos Struct 2016;140:630–43. https://doi.org/10.1016/j.compstruct.2015.12.031.

[12] Hou M, Friedrich K, Scherer R. Optimization of stamp forming of thermoplastic composite bends. Compos Struct 1994. https://doi.org/10.1016/0263-8223(94)90077-9.

[13] Donderwinkel TG, Rietman B, Haanappel SP, Akkerman R. Stamp forming optimization for formability and crystallinity. AIP Conf. Proc., 2016. https://doi.org/10.1063/1.4963585.

[14] Mayer N, Prowe J, Havar T, Hinterhölzl R, Drechsler K. Structural analysis of composite components considering manufacturing effect. Compos Struct 2016;140:776–82. https://doi.org/10.1016/j.compstruct.2016.01.023.

[15] Nino GF, Bergsma OK, Bersee HE, Beukers A. Influence of fiber orientation on mechanical

performance for thermoformed composites. ICCM Int Conf Compos Mater 2007:1–7.

[16] Kärger L, Galkin S, Zimmerling C, Dörr D, Linden J, Oeckerath A, et al. Forming optimisation embedded in a CAE chain to assess and enhance the structural performance of composite components. Compos Struct 2018;192:143–52. https://doi.org/10.1016/j.compstruct.2018.02.041.

[17] Tatsuno D, Yoneyama T, Kawamoto K, Okamoto M. Hot press forming of thermoplastic CFRP sheets. Procedia Manuf 2018;15:1730–7. https://doi.org/10.1016/j.promfg.2018.07.254.

[18] Mayer N, Van Den Broucke B, Prowe J, Havar T, Hinterhölzl R. Finite element mapping for incompatible FE meshes of composite structures. Adv Eng Softw 2016;99:81–8. https://doi.org/10.1016/j.advengsoft.2016.05.007.

[19] Kärger L, Bernath A, Fritz F, Galkin S, Magagnato D, Oeckerath A, et al. Development and validation of a CAE chain for unidirectional fibre reinforced composite components. Compos Struct 2015;132:350–8. https://doi.org/10.1016/j.compstruct.2015.05.047.

[20] Hsiao S-W, Kikuchi N. Numerical analysis and optimal design of composite thermoforming process. Comput Methods Appl Mech Eng 1999;177:1–34. https://doi.org/10.1016/S0045-7825(98)00273-4.

[21] Jayasree NA, Airale AG, Ferraris A, Messana A, Sisca L, Carello M. Process analysis for structural optimisation of thermoplastic composite component using the building block approach. Compos Part B Eng 2017;126:119–32. https://doi.org/10.1016/j.compositesb.2017.06.007.

[22] Rouse M, Jegley DC, McGowan DM, Bush HG, Waters WA. Utilization of the building-block approach in structural mechanics research. Collect Tech Pap - AIAA/ASME/ASCE/AHS/ASC Struct Struct Dyn Mater Conf 2005;2:860–78. https://doi.org/10.2514/6.2005-1874.

[23] Cao J, Akkerman R, Boisse P, Chen J, Cheng HS, de Graaf EF, et al. Characterization of mechanical behavior of woven fabrics: Experimental methods and benchmark results. Compos Part A Appl Sci Manuf 2008;39:1037–53. https://doi.org/10.1016/j.compositesa.2008.02.016.

[24] Harrison P, Wiggers J, Long AC. Normalization of shear test data for rate-independent compressible fabrics. J Compos Mater 2008;42:2315–44. https://doi.org/10.1177/0021998308095367.

[25] Lebrun G, Bureau MN, Denault J. Evaluation of bias-extension and picture-frame test methods for the measurement of intraply shear properties of PP/glass commingled fabrics. Compos Struct 2003;61:341–52. https://doi.org/10.1016/S0263-8223(03)00057-6.

[26] ASM International Handbook Committee. ASM Handbook Vol. 2: Properties and selection--nonferrous alloys and special-purpose materials. 2001. https://doi.org/10.1016/S0026-0576(03)90166-8.

[27] Radioss, Reference guide, starter input, interfaces, penalty method, /INTER/TYPE 21 n.d.

[28] Khan MA, Mabrouki T, Vidal-Sallé E, Boisse P. Numerical and experimental analyses of woven composite reinforcement forming using a hypoelastic behaviour. Application to the double dome benchmark. J Mater Process Technol 2010;210:378–88. https://doi.org/10.1016/j.jmatprotec.2009.09.027.

[29] Harrison P, Gomes R, Curado-Correia N. Press forming a 0/90 cross-ply advanced thermoplastic composite using the double-dome benchmark geometry. Compos Part A Appl Sci Manuf 2013;54:56–69. https://doi.org/10.1016/j.compositesa.2013.06.014.

[30] Peng X, Guo Z, Du T, Yu WR. A simple anisotropic hyperelastic constitutive model for textile fabrics with application to forming simulation. Compos Part B Eng 2013;52:275–81. https://doi.org/10.1016/j.compositesb.2013.04.014.

[31] Boisse P, Gasser A, Hagege B, Billoet JL. Analysis of the mechanical behavior of woven fibrous material using virtual tests at the unit cell level. J. Mater. Sci., 2005. https://doi.org/10.1007/s10853-005-5069-7.

[32] Yu WR, Pourboghrat F, Chung K, Zampaloni M, Kang TJ. Non-orthogonal constitutive equation for woven fabric reinforced thermoplastic composites. Compos Part A Appl Sci Manuf 2002. https://doi.org/10.1016/S1359-835X(02)00053-2.

[33] Peng XQ, Cao J. A continuum mechanics-based non-orthogonal constitutive model for woven composite fabrics. Compos Part A Appl Sci Manuf 2005. https://doi.org/10.1016/j.compositesa.2004.08.008.

[34] Parlevliet PP, Bersee HEN, Beukers A. Residual stresses in thermoplastic composites—A study of the literature—Part I: Formation of residual stresses. Compos Part A Appl Sci Manuf 2006;37:1847–57. https://doi.org/10.1016/j.compositesa.2005.12.025.

[35] Parlevliet PP, Bersee HEN, Beukers A. Residual stresses in thermoplastic composites-A study of the literature-Part II: Experimental techniques. Compos Part A Appl Sci Manuf 2007. https://doi.org/10.1016/j.compositesa.2006.07.002.

[36] Parlevliet PP, Bersee HEN, Beukers A. Residual stresses in thermoplastic composites - a study of the literature. Part III: Effects of thermal residual stresses. Compos Part A Appl Sci Manuf 2007. https://doi.org/10.1016/j.compositesa.2006.12.005.

[37] Barnes JA, Byerly GE. The formation of residual stresses in laminated thermoplastic composites. Compos Sci Technol 1994;51:479–94. https://doi.org/10.1016/0266-3538(94)90081-7.

[38] Agha A, Abu-Farha F. Experimental methods to capture curing induced effects in adhesive bonded joints. Int J Adhes Adhes 2021. https://doi.org/10.1016/j.ijadhadh.2020.102735.

[39] Agha A, Abu-Farha F. Viscoelastic model to capture residual stresses in heat cured dissimilar adhesive bonded joints. Int J Adhes Adhes 2021. https://doi.org/10.1016/j.ijadhadh.2021.102844.

[40] Young RJ, Day RJ, Zakikhani M, Robinson IM. Fibre deformation and residual thermal stresses in carbon fibre reinforced PEEK. Compos Sci Technol 1989;34:243–58. https://doi.org/10.1016/0266-3538(89)90031-6.

[41] Nairn JA, Zoller P. Matrix solidification and the resulting residual thermal stresses in composites. J Mater Sci 1985;20:355–67. https://doi.org/10.1007/BF00555929.

[42] Cowley KD, Beaumont PWR. The measurement and prediction of residual stresses in carbon-fibre/polymer composites. Compos Sci Technol 1997;57:1445–55. https://doi.org/10.1016/S0266-3538(97)00048-1.

[43] Jeronimidis G, Parkyn AT. Residual Stresses in Carbon Fibre-Thermoplastic Matrix Laminates. J Compos Mater 1988;22:401–15. https://doi.org/10.1177/002199838802200502.

[44] Wang C, Sun CT. Thermoelastic Behavior of PEEK Thermoplastic Composite during Cooling from Forming Temperatures. J Compos Mater 1997;31:2230–48. https://doi.org/10.1177/002199839703102201.

[45] Manson JAE, Seferis JC. Process Simulated Laminate (PSL) : A Methodology to Internal Stress

Characterization in Advanced Composite Materials. J Compos Mater 1992. https://doi.org/10.1177/002199839202600305.

[46] Chapman TJ, Gillespie JW, Pipes RB, Manson J-AE, Seferis JC. Prediction of Process-Induced Residual Stresses in Thermoplastic Composites. J Compos Mater 1990;24:616–43. https://doi.org/10.1177/002199839002400603.

[47] Bogetti TA, Gillespie JW. Process-Induced Stress and Deformation in Thick-Section Thermoset Composite Laminates. J Compos Mater 1992;26:626–60. https://doi.org/10.1177/002199839202600502.

[48] Ouyang C, Xiang X, Xue W, Gao Q, Zhao Z, Zheng K, et al. Effect of Polyamide 6 on Crystallization Nucleation Behavior and Mechanical Properties of Polyoxymethylene, 2015. https://doi.org/10.2991/icaemt-15.2015.12.

[49] Jones RM. Mechanics of Composite Materials Jones 1999. 1999. https://doi.org/10.1007/BF00611782.

[50] Agha A. Cure Dependent Viscoelastic-Plastic Modeling of Adhesives to Capture CTE Effects in Multi-Material Structures. 2019.

[51] Engel B, Böcking J. Bending of fibre-reinforced thermoplastic tubes. ICCM Int Conf Compos Mater 2015;2015-July.

[52] Whitney JM. Structural Analysis Of Laminated Anisotropic Plates. Routledge; 2018. https://doi.org/10.1201/9780203738122.

[53] Fung, Y, Tong, P, Bechtel, S. Classical and Computational Solid Mechanics. Appl Mech Rev 2003;56:B1–2. https://doi.org/10.1115/1.1523351.

[54] Matzenmiller A, Lubliner J, Taylor RL. A constitutive model for anisotropic damage in fiber-composites. Mech Mater 1995. https://doi.org/10.1016/0167-6636(94)00053-0.

[55] Hashin Z. Failure criteria for unidirectional fiber composites. J Appl Mech Trans ASME 1980. https://doi.org/10.1115/1.3153664.

[56] Hallquist J. LS-DYNA® theory manual. 2006.

[57] Hashemi S, Kinloch A, Williams G. Mixed-Mode Fracture in Fiber-Polymer Composite Laminates. Compos. Mater. Fatigue Fract. (Third Vol., 2009. https://doi.org/10.1520/stp17717s.

[58] Feraboli P, Deleo F, Wade B, Rassaian M, Higgins M, Byar A, et al. Predictive modeling of an energy-absorbing sandwich structural concept using the building block approach. Compos Part A Appl Sci Manuf 2010. https://doi.org/10.1016/j.compositesa.2010.02.012.

[59] Li A. Optimization of Composite Structures for Crashworthiness. 2019. https://doi.org/10.2514/6.1996-3999.

[60] Feraboli P, Wade B, Deleo F, Rassaian M, Higgins M, Byar A. LS-DYNA MAT54 modeling of the axial crushing of a composite tape sinusoidal specimen. Compos Part A Appl Sci Manuf 2011. https://doi.org/10.1016/j.compositesa.2011.08.004.

[61] Andersson M, Liedberg P. Crash behavior of composite structures - A CAE benchmarking study. 2014.

[62] Boria S, Pettinari S, Giannoni F, Cosimi G. Analytical and numerical analysis of composite impact attenuators. Compos Struct 2016. https://doi.org/10.1016/j.compstruct.2015.09.032.

Appendix

A1. High Temperature tensile and shear plots

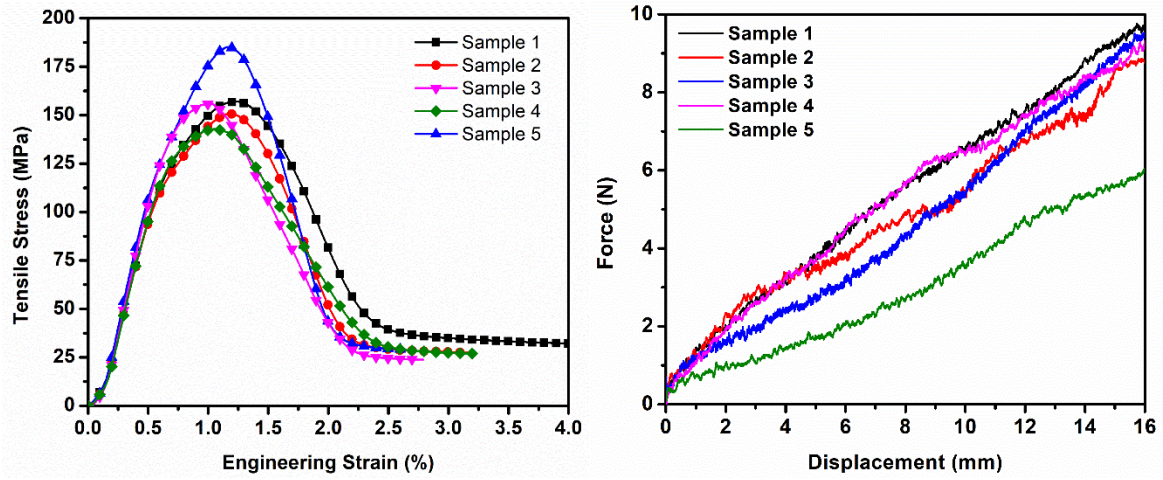

(a) (b)

Figure 1. (a) Experimental tensile load-displacement curves of PA6/Woven CF 0/90°orientation at 264 °C, (b) Experimental bias-extension load-displacement curves of PA6/Woven CF 45°orientation at 264 °C

A2. Tensile, compression and shear plots

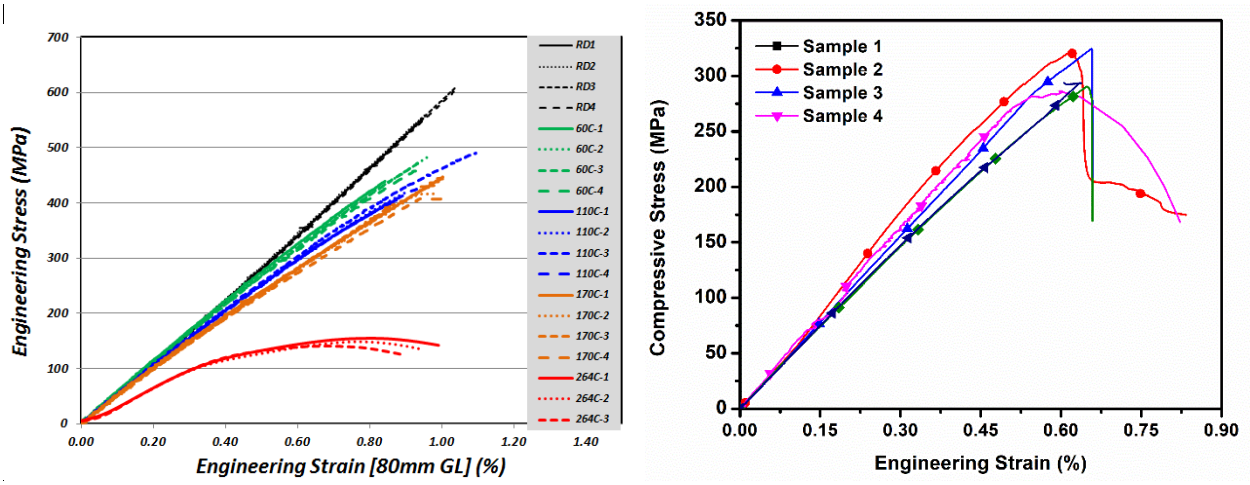

(a) (b)

Figure 2. (a) Experimental tensile stress-strain curves of PA6/Woven CF 0/90°orientation at RT, 60°C, 110°C and 170°C, (b) Experimental compressive stress-strain curves 0/90°orientation at RT.

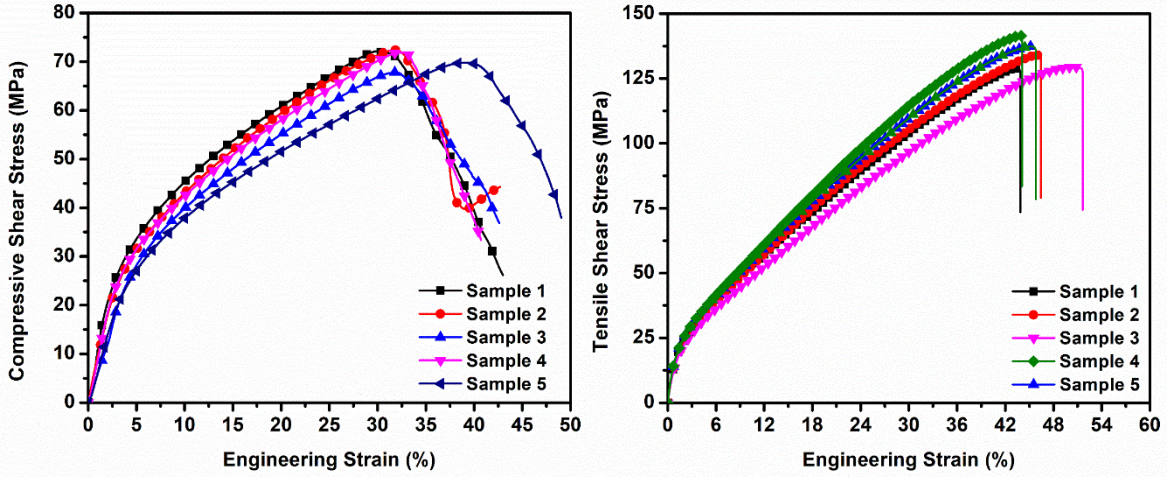

(a) *(b)*

Figure 3. (a) Experimental tensile shear stress-strain curves of PA6/Woven CF 45°orientation at RT, (b) Experimental compressive shear stress-strain curves 45°orientation at RT.

Appendix B: Details of Modeling Pathway

B1. Thermoforming simulation

The hat structure has a length of 145mm and the blank has a length of 297mm. The radius of curvature of the hat structure is 9.18mm with a width of 75mm, while the blank width is 210mm. The MAT LAW 58 model employs two local axes oriented in the two fiber directions (warp and weft) and accounts for the interaction between the warp and weft woven tows. The local axes follow the rotations of the fibers during element deformation, which enables the in-plane shear behavior.

B2. Determination of residual stresses

These residual stresses are primarily driven by the volumetric shrinkage effect during the cooling process. The temperature evolution data obtained from the transient thermal analysis is used to first deduce the 'stress-free incremental thermal strains for the *k*-th ply at a given time step *t*. The 'stress-free' herein, refers to the thermal strains developed in a ply, when it is free to deform without any constraint, which can be calculated by:

$$\begin{bmatrix} \left(\Delta\varepsilon_{x1}^{T}\right) \\ \left(\Delta\varepsilon_{x3}^{T}\right) \\ \left(\Delta\varepsilon_{x1x3}^{T}\right) \end{bmatrix}_{k} = \begin{bmatrix} \left(\varepsilon_{x1}^{T}\right)_{t} - \left(\varepsilon_{x1}^{T}\right)_{t-1} \\ \left(\varepsilon_{x3}^{T}\right)_{t} - \left(\varepsilon_{x3}^{T}\right)_{t-1} \\ \left(\varepsilon_{x1x3}^{T}\right)_{t} - \left(\varepsilon_{x1x3}^{T}\right)_{t-1} \end{bmatrix}_{k} = \begin{bmatrix} \alpha_{x1} \\ \alpha_{x3} \\ \alpha_{x1x3} \end{bmatrix} \left(\Delta T\right)_{k} \tag{5}$$

Where, $\alpha_{x1} = 1.54\frac{\mu m}{m\,℃}, \alpha_{x3} = 1.54\frac{\mu m}{m\,℃}$ and $\alpha_{x1x3} = 0$ are the in-plane thermal expansion coefficients below Tg and $\alpha_{x1} = 1.86\frac{\mu m}{m\,℃}, \alpha_{x3} = 1.86\frac{\mu m}{m\,℃}$ and $\alpha_{x1x3} = 0$ are coefficients above Tg. $(\Delta T)_k = (T_t - T_{t-1})_k$ is the temperature change for a timestep, ε is the strain, subscript x1, x3, x1x3 denotes the direction of strain, superscript T refers to thermal strain and subscript t denotes the time step. The net deformation of any given k-th ply in a laminate is dictated by the thermal and mechanical properties of all the plies in that laminate. In other words, an individual ply strain is affected by the average laminate strain. This difference between the average laminate strain and the 'stress-free ply strains (from Equation (5)) causes the residual stresses to develop in the ply. This is illustrated in the Figure 4, where a laminate structure comprised of two plies is shown. In an unconstrained state, ply 1 and ply 2, undergo 'stress-free' strains $\varepsilon_1$and ε_2 respectively. However, in the laminate setup, both plies undergo average laminate strain ε_m. Therefore, the stresses in ply1 are proportional to $\varepsilon_1 - \varepsilon_m$ and that in ply 2 are proportional to $\varepsilon_2 - \varepsilon_m$.

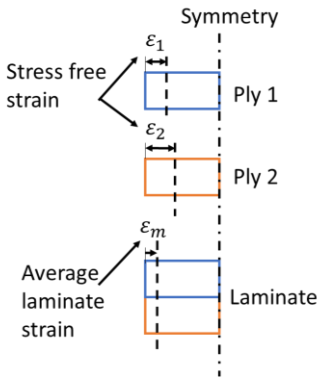

Figure 4 Illustration of stress free strains vs average laminate strain

Typically, the average laminate strains are represented by the strains occurring in the laminate midplane due to the introduction of thermal loading on the laminated structure. The thermal loading herein can be defined by the resultant forces and moments that act on the laminated structure and is expressed as the cumulative sum of thermal forces on all plies. The resultant forces on the laminate are calculated at each time step *t*, i.e. incremental resultant forces (*N*). Since, the cooling process takes place in a closed mold where the laminate is constrained in all directions, therefore, out-of-plane deformations within the plies do not exist. Consequently, the curvatures and moments are neglected, and the incremental resultant forces are expressed in a simplified form as [49]:

$$\begin{bmatrix} \Delta N_{x1}^{T} \\ \Delta N_{x3}^{T} \\ \Delta N_{x1x3}^{T} \end{bmatrix} = \begin{bmatrix} \left(N_{x1}^{T}\right)_{t} - \left(N_{x1}^{T}\right)_{t-1} \\ \left(N_{x3}^{T}\right)_{t} - \left(N_{x3}^{T}\right)_{t-1} \\ \left(N_{x1x3}^{T}\right)_{t} - \left(N_{x1x3}^{T}\right)_{t-1} \end{bmatrix} = \sum_{k=1}^{nn} \left\{ \begin{bmatrix} \overline{Q}_{11} & \overline{Q}_{12} & \overline{Q}_{16} \\ \overline{Q}_{12} & \overline{Q}_{22} & \overline{Q}_{26} \\ \overline{Q}_{16} & \overline{Q}_{26} & \overline{Q}_{66} \end{bmatrix}_{k} \begin{bmatrix} \Delta\varepsilon_{x1}^{T} \\ \Delta\varepsilon_{x3}^{T} \\ \Delta\varepsilon_{x1x3}^{T} \end{bmatrix} \int_{h_{k-1}}^{h_k} dx2 \right\} \tag{6}$$

Where, $\bar{Q}_{ij} = \bar{Q}_{ij}(T), \{i, j = 1, 2, 6\}$plane stress stiffness matrix which is defined [52] in terms of the engineering properties and is temperature-dependent. Now the incremental laminate strain or the laminate mid-plane strain can be calculated at time step *t*, by following the laminate constitutive relationship as [49]:

$$\begin{bmatrix} \Delta\varepsilon_{x1}^{0} \\ \Delta\varepsilon_{x3}^{0} \\ \Delta\varepsilon_{x1x3}^{0} \end{bmatrix} = \begin{bmatrix} \left(\varepsilon_{x1}^{0}\right)_{t} - \left(\varepsilon_{x1}^{0}\right)_{t-1} \\ \left(\varepsilon_{x3}^{0}\right)_{t} - \left(\varepsilon_{x3}^{0}\right)_{t-1} \\ \left(\varepsilon_{x1x3}^{0}\right)_{t} - \left(\varepsilon_{x1x3}^{0}\right)_{t-1} \end{bmatrix} = [\mathbf{A}]^{-1} \begin{bmatrix} \Delta N_{x1}^{T} \\ \Delta N_{x3}^{T} \\ \Delta N_{x1x3}^{T} \end{bmatrix} \tag{7}$$

where, $\Delta\boldsymbol{\varepsilon}^{\mathbf{0}}$ represents increments in laminate midplane strain from the previous time step. The matrix **A** is the 3-by-3 in-plane stiffness matrix for the laminate. It is worthwhile to note that, the coupling factor in the stiffness matrix is neglected herein, since a balanced layup is considered. The coefficient of the **A** matrix is given by, $A_{ij} = \sum_{k=1}^{nn} \left(\bar{Q}_{ij}\right)_{k} e_k$.

The stress transformation can be expressed for *k*-th ply as:

$$\begin{bmatrix} \sigma_x \\ \sigma_y \\ \sigma_z \\ \sigma_{yz} \\ \sigma_{xz} \\ \sigma_{xy} \end{bmatrix}_{k} = \begin{bmatrix} c^2 & s^2 & 0 & 0 & 0 & -2sc \\ s^2 & c^2 & 0 & 0 & 0 & 2sc \\ 0 & 0 & 1 & 0 & 0 & 0 \\ 0 & 0 & 0 & c & s & 0 \\ 0 & 0 & 0 & -s & c & 0 \\ sc & -sc & 0 & 0 & 0 & c^2 - s^2 \end{bmatrix} \begin{bmatrix} \sigma_{x1} \\ 0 \\ \sigma_{x3} \\ 0 \\ \sigma_{x1x3} \\ 0 \end{bmatrix}_{k} \tag{8}$$

Where c denotes $\cos(\theta)$ and s denotes $\sin(\theta)$. This analysis was repeated for all other discretized laminates along the cross-section profile since the through-thickness temperature gradient could be different at different locations.